

Revised Parameterization of Air–Sea Exchanges in High Winds for Operational Numerical Prediction: Impact on Tropical Cyclone Track, Intensity, and Rapid Intensification

YIMIN MA, NOEL E. DAVIDSON, AND YI XIAO

Centre for Australian Weather and Climate Research,^a Melbourne, Victoria, Australia

JIAN-WEN BAO

NOAA/ESRL, Boulder, Colorado

(Manuscript received 21 August 2015, in final form 16 December 2016)

ABSTRACT

In high-wind conditions, sea spray, in conjunction with a generally decreasing drag coefficient for increasing winds, greatly modulates surface heat and momentum fluxes. It has been suggested that the process can be particularly important for the prediction of tropical cyclones (TCs), yet its robust application in operational forecast systems has remained elusive. A sea spray inclusion scheme and a modified algorithm for momentum exchange have been implemented in the Australian Bureau of Meteorology's current operational TC model. Forecasts for a limited sample of TCs demonstrate that the revised parameterizations improve initialized and forecast intensities, while mostly maintaining track prediction skill. TC Yasi (2011) has been studied for impacts of the revised parameterization on rapid intensification (RI). Compared with the conventional bulk air–sea exchange parameterization, the revised version simulates a cooler and moister region near the surface in the eyewall/eye region, adjusts the RI evolution by an earlier and stronger subsidence in the eye, and simulates a stronger radial pulsating of the eye and eyewall convection on relatively short time scales. The inclusion of the new scheme enhances RI features characterized by eyewall ascent, radial convergence, and inertial stability inside the radius of azimuthal-mean maximum wind over low- to midlevels, and by a ringlike radial distribution of relative vorticity above the boundary layer. In addition, it allows a higher maximum intensity wind speed based on Emanuel's maximum potential intensity theory. It is shown that, as expected, this is mainly because of a larger ratio of enthalpy and momentum exchange coefficients.

1. Introduction

Energy for the genesis and development of tropical cyclones (TCs) is essentially supplied by heat and moisture from the tropical oceans. Energy exchange at the air–sea interface, as discussed for example in Black et al. (2007), is one of the three major physical processes governing hurricane intensity change, together with 1) environmental interactions with surrounding large-scale circulations and 2) internal dynamics such as eyewall replacement cycles and cloud microphysics. Precise representation of the air–sea energy exchange is crucial for TC forecasting

and, particularly, for prediction of intensity and structure change, with the latter on occasions further affecting the track. It is thus important to represent the air–sea exchanges as best we can. Furthermore, the coherent relationship between the air–sea interaction and the internal dynamics during hurricane intensity change remains mostly unexplained, and so a better representation of the surface processes will help us to understand TC development in an integrated way.

The energy exchanges are composed of momentum, sensible heat, and latent heat (moisture) fluxes. Over water, a “bulk” exchange parameterization is commonly applied in numerical modeling to compute the fluxes in TC models. The fluxes are parameterized as being proportional to exchange coefficients and the differences in wind, temperature, and moisture between the surface and lowest model level in the boundary layer (e.g., Fairall et al. 2003). The exchange coefficient for momentum flux,

^aThe Centre for Australian Weather and Climate Research is a partnership between the Commonwealth Scientific and Industrial Research Organisation and the Bureau of Meteorology.

Corresponding author e-mail: Yimin Ma, yma@bom.gov.au

or drag coefficient, plays a role not only in parameterization for the momentum flux but also for the heat exchanges, because the turbulent heat exchanges also rely on near-surface wind shear. The drag coefficient over water was initially based upon the Charnock relation with a constant Charnock parameter (Charnock 1955). However, based on the analysis of results from field programs, a constant Charnock parameter is questionable. Wu (1980) has reviewed the derivation of the Charnock parameter and obtained values with a large range from 0.012 to 0.035 at moderate ($>5 \text{ m s}^{-1}$) to strong wind speeds. Fairall et al. (2003) recommended a relationship between the Charnock parameter and the 10-m near-surface wind speed in neutral conditions. This was termed the COARE3.0 (Coupled Ocean–Atmosphere Response Experiment; e.g., Fairall et al. 2003) expression and was based upon analysis of large sets of data from field programs. They also pointed out that the variation of the Charnock parameter with wind speed still remains uncertain. Although the Charnock parameter has been related to ocean wave age, as functions of the ratio of the wave phase speed at the peak of the spectrum and either the friction velocity or the 10-m neutral wind speed U_{10N} (Drennan et al. 2005; Donelan 1982), Fairall et al. (2003) pointed out that there is still a lack of consensus on the relationship in the wave stress community. Andreas et al. (2012) endorsed a correlation between the surface friction velocity and U_{10N} , which is equivalent to a correlation between a variable Charnock parameter and the winds, using data for winds up to 24 m s^{-1} . At very high wind speeds near the hurricane eyewall ($>40 \text{ m s}^{-1}$), Powell et al. (2003) obtained a declining drag coefficient with increasing near-surface winds using global positioning system (GPS) sondes. Focusing on the hurricane component of the Coupled Boundary Layers Air–Sea Transfer experiment (CBLAST), Black et al. (2007) also obtained a declining drag coefficient even when the winds were greater than 25 m s^{-1} (their Fig. 5). Based on a laboratory experiment, Donelan et al. (2004) suggested that the coefficient tends to level off when the winds are greater than 35 m s^{-1} . Bell et al. (2012) obtained a declining or nonincreasing drag coefficient when the winds were greater than 60 m s^{-1} . The latter study computed quite scattered values of the coefficient by deducing the momentum and enthalpy fluxes via absolute angular momentum and total energy budgets. Although the methodology and data used to obtain the coefficient at very high wind speeds are problematic, the mechanisms behind the phenomena have been discussed. For instance, Powell et al. (2003) speculate that sea foam and sea spray generated by wave breaking and wind tearing the breaking wave chest prevent the underlying sea surface from being dragged by the

wind. Physical models were being set up to illustrate and simulate the phenomena (e.g., Liu et al. 2012; Makin 2005).

At high winds, the concept of a thermal roughness length for sensible and latent heat fluxes is no longer fully valid. At low winds, heat and water vapor at the air–sea interface are transferred by molecular diffusion across an interfacial sublayer (e.g., Garratt 1994, p. 89), which is then defined as the *interfacial route*. As one of several physical mechanisms proposed, a cyclic growth and destruction pattern of the interfacial sublayer accounts for the introduction of the thermal roughness length (Liu and Businger 1975). At higher winds ($>10 \text{ m s}^{-1}$), heat and water vapor transfers also occur at the surface of the spray droplets, which have been blown up through the interfacial sublayer, which is then defined as the *spray route* for heat and water vapor exchanges (e.g., Andreas et al. 2008). Parameterizations for the spray route have been developed by Andreas et al. (2008), Andreas (2010), Fairall et al. (1994), Fairall et al. (2009), Kepert et al. (1999), and Bao et al. (2011).

Using two spray route inclusion schemes, Wang et al. (2001) made a simulation of a TC and analyzed the influence on the TC boundary layer structure. Bao et al. (2000) used an air–sea coupled model that included wave and spray models to make a study of TC development. Neither of the studies made simulations of real TCs. These studies were essentially for research purposes; the feasibility of the application of a sea spray parameterization to operational tropical cyclone models is thus yet to be fully investigated.

Through theoretical considerations, Emanuel (1986) proposed that air–sea sensible and latent heat fluxes are more critical in developing and maintaining a TC than the ambient air instability. Emanuel (1986, 1995), with further revision to the theory, suggested a relationship between the maximum tangential wind speed averaged over the subcloud layer and the ratio of enthalpy to momentum exchange coefficients for a steady-state TC, based on the balance between radial entropy advection and surface entropy flux over the inner region of a TC in quasi-equilibrium. This leads to a constraint on the ratio of the coefficients for TC conditions. How the ratio behaves with the new surface exchange parameterization is one of the issues addressed in this study. Our preliminary results indicate some consistency with the theoretical predictions. The focus of this study is on the revised parameterizations and their impact on TC predictions, and particularly rapid intensification (RI). A summary of TC studies on structure and intensity can be found in Wang and Wu (2004). In addition, we will discuss other aspects of RI in the text.

In summary, in high winds, the parameterizations for each of the momentum and heat exchanges at the

air–sea interface are quite different from the conventional bulk exchange algorithms, as evidenced from various observational studies. Clearly, it is of great significance to the TC numerical weather prediction (NWP) and air–sea exchange research communities that a spray route inclusion scheme be applied to operational TC forecast systems. Documenting its potential impact on TC track, intensity, and internal dynamics—especially the intensification process—is then of theoretical and practical interest. We have thus investigated the impact of a new parameterization on TC forecasts in the current Australia TC model.

The manuscript is organized as follows. Section 2 summarizes the parameterizations for air–sea exchanges, which comprise a conventional bulk algorithm, a spray route inclusion scheme at high wind speeds, and a surface-wind-dependent Charnock relation. Section 3 briefly describes a TC model that has been applied to evaluate the new scheme. Section 4 offers a discussion on the TC track and intensity evaluations and provides an illustrative example of a TC rapid intensification case with some detailed diagnostics. Section 5 provides our conclusions.

2. Air–sea exchange parameterization

a. Bulk air–sea exchange parameterization in the UM

The experiments described here use the Met Office Unified Model, version UM6.4, which will be briefly described in section 3. Bulk surface flux parameterizations are used for surface momentum and heat fluxes exchanges. Based on Monin–Obukhov similarity theory (MOST; e.g., Garratt 1994, p. 38), “bulk” algorithms for estimating the air–sea interface fluxes for momentum τ_0 and sensible (SH) and latent heat (LH) can be expressed as (e.g., Lock 2007)

$$\tau_0 = \rho_a C_D V \mathbf{u}_{z_1}, \tag{1a}$$

$$\text{SH} = -\rho_a c_{pa} \left\{ C_H V \left[(T_{z_1} - T_{z_{0h}}) + \frac{g}{c_{pa}} (z_1 - z_{0m} - z_{0h}) \right] \right\}, \tag{1b}$$

and

$$\text{LH} = -\rho_a L_v C_H V (q_{z_1} - q_{z_{0h}}), \tag{1c}$$

where \mathbf{u} , T , and q are the wind speed, air temperature, and specific humidity, respectively, and the subscripts z_1 and z_{0h} denote the variables at these heights. We use z_{0m} and z_{0h} to represent the momentum and thermal

roughness lengths, respectively. The latent heat of vaporization is L_v , the air density near the surface is ρ_a , the specific heat for air is c_{pa} , and the gravitational acceleration is g . Effective wind speed for surface turbulence V is defined as $V = v_*/\sqrt{C_D}$, where v_* is the surface scaling velocity defined by the relation $v_*^2 = u_*^2 + \beta^2 w_*^2$. In this relation, u_* is the surface friction velocity and w_* is the convective velocity scale. In addition, β is a constant and set to zero in neutral and stable conditions.

Surface exchange coefficients for momentum flux (drag coefficient C_D) and sensible and latent heat fluxes C_H are defined, respectively, as

$$\sqrt{C_D} = \frac{\kappa}{\ln(z_1/z_{0m}) + \Psi_m(L, z_1 + z_{0m}, z_{0m})} \quad \text{and} \tag{2a}$$

$$C_H = \frac{\kappa}{\ln(z_1/z_{0h}) + \Psi_h(L, z_1 + z_{0m}, z_{0h})} \sqrt{C_D}, \tag{2b}$$

where κ is von Kármán’s constant and L is the Monin–Obukhov length. The empirical functions Ψ_m and Ψ_h are used as stability corrections. Note that C_D affects both the momentum and heat fluxes through V in Eqs. (1a) and (1c).

Accuracy of the roughness lengths z_{0m} and z_{0h} in the bulk algorithm contributes as one of the major sources of uncertainty in the derivation of surface fluxes in numerical modeling over oceans. The momentum roughness length z_{0m} determines the exchange coefficient C_D through Eq. (2a) and affects the momentum and heat fluxes through Eqs. (2b), (1b), and (1c). Over water, the conventional momentum roughness length z_{0m} mainly follows the Charnock relation (Charnock 1955) and has a dependence on the surface friction velocity u_* as (e.g., Smith 1988)

$$z_{0m} = \frac{0.11\gamma}{b + u_*} + \frac{\alpha}{g} u_*^2, \tag{3}$$

where the first term represents an aerodynamically smooth flow at low wind speeds and the second term represents the original Charnock relation. In Eq. (3), γ is the kinematic viscosity, b is a constant and represents a limit that z_{0m} can reach at $u_* = 0$, and α is normally treated as a constant and termed the Charnock constant or Charnock parameter. At high winds Eq. (3) is approximated by the original Charnock relation of $z_{0m}g/u_*^2 = \alpha$. In UM6.4, we take α as 0.018. The choice of this parameter is further discussed in the next section.

Edwards (2007) derived the following expressions for UM6.4 for the thermal roughness length:

$$z_{0h} = \begin{cases} \max\left(\frac{2.52 \times 10^{-6}}{u_* + b}, \frac{2.56 \times 10^{-9}}{z_{0m}}\right) & \text{Low wind condition} \\ \max\left(\frac{2.56 \times 10^{-9}}{z_{0m}}, 7 \times 10^{-8}\right) & \text{High wind condition} \end{cases} \quad (4)$$

As winds become calm, the thermal roughness length is similar to that of the momentum roughness length (Large and Pond 1982). Csanady (2001) suggests a relation that the product $z_{0h}z_{0m}$ is a constant that is supported with a dimensional analysis. By adopting this relation, Edwards (2007) determined the constant from a value of a neutral coefficient for moisture exchange at a certain wind speed, on the basis of Humidity Exchange over the Sea (HEXOS) data (e.g., Smith et al. 1992). Such a formulation improves the simulation of the global general circulation (Edwards 2007), compared to the use of a constant z_{0h} in the older version of the UM.

b. The BFK sea spray parameterization scheme for air–sea heat and moisture exchanges

The spray route inclusion scheme is based on a series of studies reported upon in Bao et al. (2011), Fairall et al. (1994), and Kepert et al. (1999). That work led to a method we call the BFK scheme, although in fact it is also based or related other works such as Andreas and Emanuel (2001) and Andreas (1992). We briefly describe the scheme in this section. The scheme consists of the parameterization of sea-spray-modulated heat and moisture fluxes at the air–sea interface. To use the scheme, we also introduce an expression for the dependence of the Charnock parameter on the 10-m wind speed in neutral conditions, and in turn the formulation of the surface roughness length over water [Eq. (3)]. We describe this expression in section 2c.

The droplet evaporation layer is defined as a layer above the sea surface where sea spray is injected into the air, and most of the heat and moisture transfer is mediated by the spray (Andreas et al. 2008). This layer typically extends about one significant wave height above mean sea level (Van Eijk et al. 2001). At or above the top of the droplet evaporation layer, sensible and latent heat fluxes have contributions from interfacial and spray routes and can be expressed as in Bao et al. (2000):

$$\text{SH} = H_S + Q_S - Q_L + H_{S,\text{eps}} \quad \text{and} \quad (5a)$$

$$\text{LH} = H_L + Q_L, \quad (5b)$$

where H_S and H_L are the sensible and latent heat fluxes through the interfacial sublayer, respectively, and Q_S and Q_L are the sensible and latent heat fluxes from spray droplets to the droplet evaporation layer, respectively. The dissipative heating converted from turbulent kinetic

energy in the atmospheric surface layer is $H_{S,\text{eps}}$. It is represented as the product of the magnitude of the surface stress and the average wind speed within the surface layer (Zhang and Altshuler 1999). Bao et al. (2011) show

$$H_S = \rho_a c_{pa} C_H V [T_s - (T_a + \delta T_a)] \quad \text{and} \quad (6a)$$

$$H_L = \rho_a L_v C_H V [q_s(T_s) - q_s(T_d + \delta T_d)] \quad (6b)$$

and

$$Q_S = \rho_w c_{pw} F_M [T_s - (T_w + \delta T_w)] \quad \text{and} \quad (7a)$$

$$Q_L = \rho_w L_v F_E [q_s(T_a + \delta T_a) - q_s(T_d + \delta T_d)], \quad (7b)$$

where T_a is the ambient air temperature, T_s is the sea surface temperature, T_w is the wet-bulb temperature, T_d is the dewpoint temperature, c_{pw} is the heat capacity for seawater, ρ_a is the air density, and ρ_w is the density of seawater. The spray water mass and water vapor fluxes are F_M and F_E , respectively. Both factors, F_M and F_E , are from the droplet spectrum (Fairall et al. 1994). There are uncertainties in their determination. We use δT_a and δT_d to show increments of near-surface atmospheric temperature and dewpoint temperature, respectively, that are due to latent heat release of the liquid sea spray droplets into the air, which basically increases the air moisture in the spray-saturated layer and decreases the temperature by absorbing the heat for droplet evaporation. Both δT_a and δT_d are determined as described in Bao et al. (2011) with extended Monin–Obukhov similarity theory based on an enthalpy budget at the air–sea interface in the presence of sea spray in the near-surface layer over water.

The interfacial fluxes [Eq. (6)] are determined by conventional methods as described in section 2a. The thermal roughness length z_{0h} is adapted from the COARE3.0 formulation (Fairall et al. 2003) as

$$z_{0h} = \min(1.1 \times 10^{-5}, 5.5 \times 10^{-5} R_e^{-0.6}) \quad (8)$$

and the Reynolds number is $R_e = u_*^* z_{0m} / \gamma$, where again γ is the kinematic viscosity. The adaptation for momentum roughness length is described in the next section.

c. Revised Charnock relation

As discussed in the introduction, it has been recognized that a constant value of the Charnock parameter α does not adequately describe the observations from many

datasets. Determining the sea surface wind stress over the open sea for a large range of surface wind speeds (6–26 m s⁻¹), [Yelland and Taylor \(1996\)](#) concluded that α monotonically increases from 0.011 to 0.017 with increasing wind speed, using an inertial dissipation method (e.g., [Fairall and Larsen 1986](#)). [Fairall et al. \(2003\)](#) derived a similar relation, COARE3.0, upon a large survey of field program results, but also pointed out that the dependence of the Charnock parameter on wind speed remains uncertain. They attribute the uncertainty upon [Yelland et al.'s \(1998\)](#) reanalyses on the results reported in [Yelland and Taylor \(1996\)](#). [Yelland et al. \(1998\)](#) no longer support the increase in α after revising with corrections to the mean winds and the measurement heights in their experiment. However, results from [Andreas et al. \(2012\)](#), who included more data from field programs conducted during recent years, are consistent with a variable Charnock parameter, dependent on U_{10} , as indicated equivalently by the correlation between u_* and U_{10N} .

For high winds, a constant Charnock parameter independent of surface wind speed leads to large biases in the drag coefficient, compared with observations. The constant Charnock parameter leads to an approximately linear increment in the drag coefficient with increasing surface winds [Eq. (2a)]. [Powell et al. \(2003\)](#) found that the drag coefficient even decreased with increasing wind speed above 40 m s⁻¹ in tropical cyclones, based on analysis of 331 GPS sonde wind profiles in 15 tropical cyclones. Those authors attributed the causes for the small roughness length to helical rolls/foams in very high winds. [French et al. \(2007\)](#) also found a decrease in the drag coefficient at high speeds using direct aircraft measurements. Their results do not match with extrapolation of the empirical forms from [Smith \(1980\)](#) and [Large and Pond \(1982\)](#), whose results increase almost linearly with increasing wind speeds.

Based on the above summary of the behavior of the Charnock parameter, we set

$$\alpha = \begin{cases} 0.011 & U_{10N} \leq 10 \text{ m s}^{-1} \\ 0.011 + \frac{0.018 - 0.011}{18 - 10} (U_{10N} - 10) & 10 < U_{10N} \leq 18 \text{ m s}^{-1}, \\ (2 \times 10^{-6} - 0.02342) \frac{\tanh[0.05(U_{10N} - 30)] + 1}{2} + 0.02342 & U_{10N} > 18 \text{ m s}^{-1} \end{cases}, \quad (9)$$

where U_{10N} is the 10-m wind speed in neutral condition. [Figure 1](#) shows the dependences of the Charnock parameter and drag coefficient on the 10-m wind speeds, for both the empirical forms and the result from existing field experiments. As shown in [Fig. 1a](#), at $U_{10N} \leq 18 \text{ m s}^{-1}$, the form is identical to COARE3.0 ([Fairall et al. 2003](#)). At $U_{10N} > 18 \text{ m s}^{-1}$, the form departs from COARE3.0 and decreases with increasing wind in neutral conditions. The new form is more consistent with the observational results of [Powell et al. \(2003\)](#) and [Donelan et al. \(2004\)](#), for the range between 30 and 50 m s⁻¹, and within low range from [Bell et al. \(2012\)](#) for very high winds (>50 m s⁻¹). The new form shows a similar trend with wind speed to the empirical formula in [Andreas et al. \(2012\)](#). The Charnock expression corresponds to a drag coefficient that is monotonically decreasing at $U_{10N} > 50 \text{ m s}^{-1}$ as shown in [Fig. 1b](#).

3. ACCESS-TC

The Australian Community Climate and Earth-System Simulator (ACCESS; [Puri et al. 2013](#)) is an implementation at the Australian Bureau of Meteorology of the full Met Office Numerical Modeling System of the United Kingdom (e.g., [Gregory and Rowntree 1990](#); [Wilson and Ballard 1999](#);

[Webster et al. 2003](#); [Davies et al. 2005](#); [Rawlins et al. 2007](#)). ACCESS-TC, its configuration for operational TC forecasting, has been adapted for operational and research applications on tropical cyclones. [Table 1](#) lists the major features of ACCESS-TC ([Davidson et al. 2014](#)). The base system runs at a resolution of 0.11° and 50 levels. The domain is relocatable and nested in coarser-resolution ACCESS forecasts. Initialization consists of five cycles of four-dimensional variational data assimilation (4DVAR) over 24 h prior to the initial time and forecasts to 72 h are made. Vortex specification or a TC bogus is applied, without which initial conditions usually contain a weak and misplaced circulation. Significant effort has been devoted to building physically based, synthetic inner-core structures, validated using historical dropsonde data and surface analyses from the Atlantic. Based on estimates of central pressure and storm size, vortex specification is used to filter the analyzed circulation from the original analysis, construct the inner core of the storm, locate it to the observed position, and merge it with the large-scale analysis at outer radii.

Using all available conventional observations and only synthetic surface pressure observations from the idealized vortex to correct the initial location and structure of the storm, 4DVAR builds a balanced, intense 3D vortex with

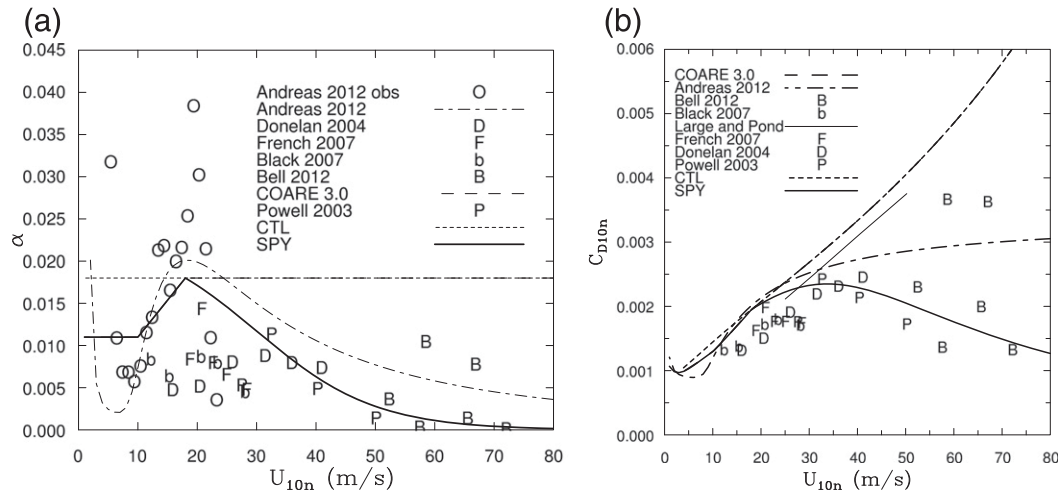


FIG. 1. Comparison of coefficients for momentum exchange parameterization for (a) Charnock parameters and (b) surface exchange coefficients, as a function of 10-m neutral wind speed. The form used in this study (SPY) is in comparison with COARE3.0 (Fairall et al. 2003; Powell et al. 2003; Large and Pond 1982; French et al. 2007; Donelan et al. 2004; Bell et al. 2012; Andreas et al. 2012) and CTL (the UM model; Lock 2007). Note that in both (a) and (b) the COARE3.0 curve is overlapped with the SPY curve at $U_{10N} < 18 \text{ m s}^{-1}$ and with the CTL curve at $U_{10N} > 18 \text{ m s}^{-1}$.

maximum wind at the radius of maximum wind and with a well-developed secondary circulation. The TC domain is one-way nested in the ACCESS global model (Puri et al. 2013). Operational estimates of TC characteristics (location, surface center pressure, and size) are derived from standard observational data and satellite image interpretation. Mean track and intensity errors for the Australian region and northwest Pacific storms have been encouraging, as are results from operational runs at the Australian National Meteorological and Oceanographic Centre. The system became fully operational in November 2011. A detailed description of the system is contained in Davidson et al. (2014).

4. Results and discussion

The revised parameterization acts in a clearly different way in simulating the fluxes from the conventional scheme.

With the distinguishing acronym of SPY (spray in combination with reduced drag in high wind speeds) and CTL (control) for the two parameterizations, Fig. 2 shows an example of exchange coefficients and fluxes along with the neutral 10-m surface wind in conditions when the sea surface is 2°C warmer than the 2-m air temperature and the relative humidity is 80% near the surface. The exchange coefficients are shown in Fig. 2a. Note for the revised parameterization that $C_{H,SPY}$ and $C_{Q,SPY}$ do not appear as a single coefficient in the formulations based on the computed fluxes from Eq. (5) for the spray route inclusion scheme. They are equivalent to the exchange coefficients that are computed with the conventional bulk formulas in Eqs. (1b) and (1c) with the heat fluxes computed from the spray route inclusion model [Eq. (5)] and the prescribed values of the difference between the near-surface air and the surface temperature, as well as

TABLE 1. Major components of ACCESS-TC.

Resolution	$0.11^\circ \times 50$ levels, 300×300 grid, relocatable with TC near center of domain
Vortex specification	1) Based on observed location, central pressure, and size; uses an analytic surface pressure profile (amended Chen and Williams 1987), tuned using 6000 dropsonde observations from the Atlantic (H. C. Weber 2010, personal communication; Davidson et al. 2014) 2) Synthetic mean sea level pressure (MSLP) obs only are used in the 4DVAR to relocate the storm to its observed location and to define the inner-core circulation; based on these relatively few MSLP obs, the 4DVAR defines the horizontal structure (max wind at the RMW, radius to gales), builds the vertical structure, and imposes a steering flow consistent with past motion
4DVAR assimilation and TC initialization	Five cycles of 4DVAR over 24 h, using all available obs data, and synthetic MSLP obs UM6.4 from ACCESS makes the forecast
Forecast	72-h forecast progressively every 12 h
Vortex tracker and diagnostics	Forecast track, structure, intensity, and other diagnostics

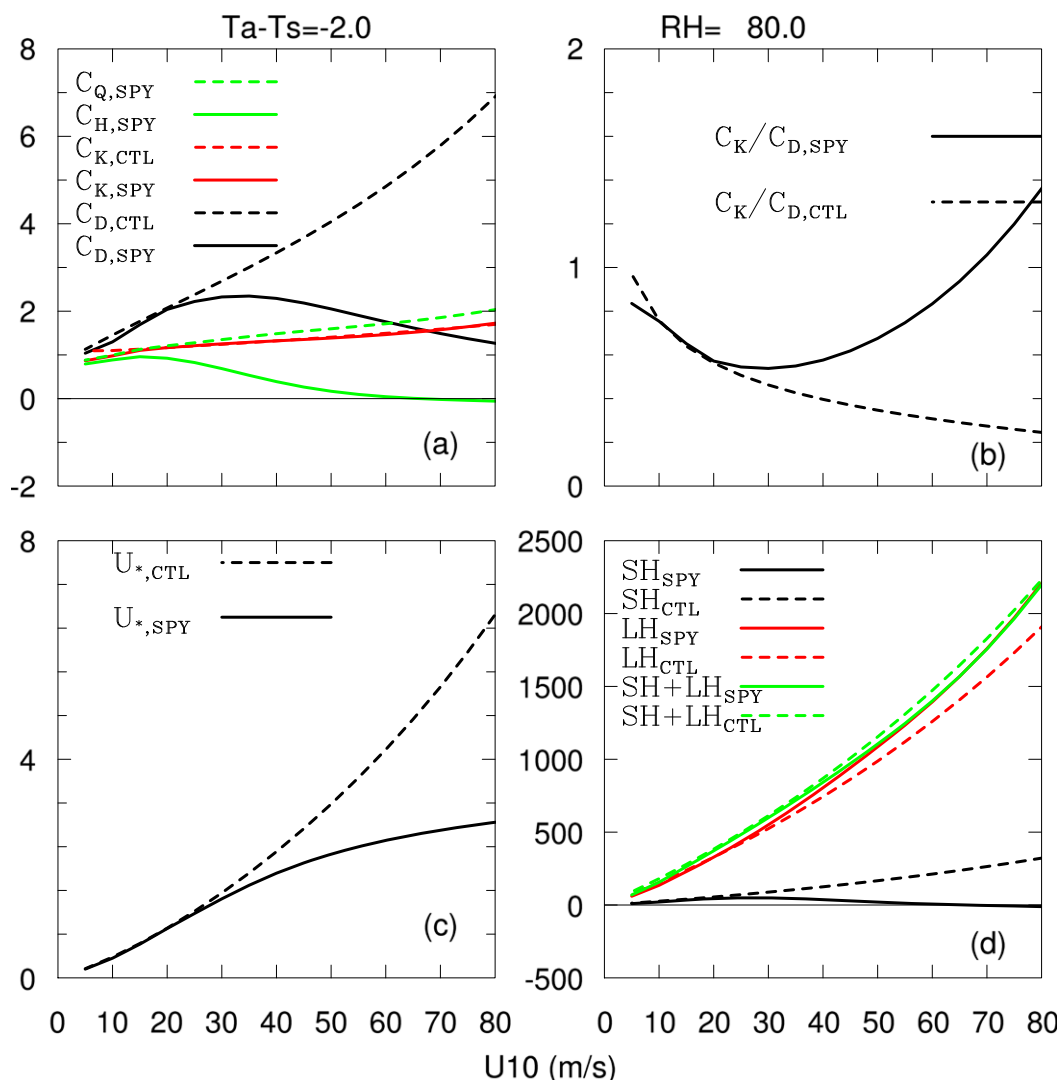


FIG. 2. The formulated exchange coefficients and fluxes for the SPY and CTL formulations: (a) C_D ($\times 10^{-3}$), C_H ($\times 10^{-3}$), C_Q ($\times 10^{-3}$), and C_K ($\times 10^{-3}$) exchange coefficients; (b) C_K/C_D ; (c) U_* ($m s^{-1}$); and (d) SH, LH, and enthalpy flux SH + LH ($W m^{-2}$).

the near-surface air relative humidity. Also note that for the original bulk scheme the thermal exchange coefficients for the sensible heat, latent heat, and enthalpy fluxes are equal ($C_{H,CTL} = C_{Q,CTL} = C_{K,CTL}$) as a thermal roughness length formulation is used for both the sensible and latent heat fluxes [Eq. (4)]. When winds are below $15 m s^{-1}$, the thermal exchange coefficients (C_H, C_Q, C_K) for the spray route inclusion scheme are not greatly different from their counterparts for the bulk scheme. When winds become high, $C_{Q,SPY}$ becomes increasingly larger while $C_{H,SPY}$ becomes increasingly smaller. The dipping of $C_{H,SPY}$ with increasing winds above about $20 m s^{-1}$ is presumably due to the cooling effect of the sea spray on the near-surface air [Eq. (5)]. Consequently, the ratio between the enthalpy exchange coefficient and drag coefficient (C_K/C_D) shows

great departures between the two parameterizations for winds greater than $20 m s^{-1}$. Results for $C_K/C_{D,SPY}$ show increasing values along with the increasing winds when they are greater than $25 m s^{-1}$, while $C_K/C_{D,CTL}$ keeps the decreasing trend. Andreas (2011) also indicates a similar large ratio using their spray model under more diverse conditions (his Fig. 3). Equivalent to the variable Charnock parameter, the friction velocity starts to be increasingly different from the original bulk formulation when winds are larger than $30 m s^{-1}$ (Fig. 2c), in agreement with the observations of Powell et al. (2003). In accordance with the difference in the exchange coefficients, as shown in Fig. 2d, the differences in the sensible and latent heat fluxes between the two schemes becomes progressively larger as winds become greater than $25 m s^{-1}$, and the

TABLE 2. Descriptions of TC case studies.

TC	No. of runs	Region of appearance	Status
Yasi (2011)	7	Australian Pacific Ocean	Intensifying with a rapidly intensifying phase and decaying with landfall
Fanapi (2010)	1	Northwest Pacific	Intensifying and decaying with landfall
Songda (2011)	4	Northwest Pacific	Intensifying and decaying with landfall
Carlos (2011)	1	Australian Indian Ocean	Steady with offshore movement

difference of their sum or enthalpy flux is comparably small. That is, for the new scheme, the moisture flux is larger and the sensible flux is smaller than for the original scheme, but the enthalpy flux remains similar.

The revised air–sea exchange parameterization schemes are thus applied in ACCESS-TC, together with the original scheme to make simulations. Table 2 shows the selected four TCs for which a total of 13 forecasts were performed for each of the two schemes. Each forecast runs for 72 h. Among the four TCs, two (Fanapi and Songda) occurred over the northwest Pacific Ocean: one (Yasi) to the northeast of Australia over the Pacific Ocean and another (Carlos) to the northwest of Australia over the eastern Indian Ocean. This represents an important geographical diversity. Two TCs (Fanapi and Songda) intensified before landfall, one (Yasi) intensified and decayed, and one (Carlos) was nearly steady with offshore movement. Figures 3 and 4 show examples of the track and intensity forecasts from each TC. Note that each figure shows the model domain. For all TCs, their major movement and curvature are well simulated with both the CTL and SPY tests. This can be attributed to the well-forecast environmental steering flow and, to a lesser extent, the vortex structure. The track errors show the differences between CTL and SPY tests and do not display large or systematic differences from these examples, although we will discuss the statistics further. The central pressures (CPs) more closely correspond with the estimates in the SPY tests than in the CTL tests for the intensification of Yasi, Fanapi, and Songda. For Carlos, which was near steady in intensity with movement away from the coast, the forecasts are similar. It is worth noting that excessive development or intensification is not a characteristic of the new scheme, even though it does represent somewhat larger latent heat fluxes.

a. Statistical analysis of predicted TC tracks and intensities

Statistically, over all of the 72-h forecasts, for both parameterizations, the average predicted track shows very similar mean errors (MEs) prior to 48 h, but the results are very marginally worse with the SPY scheme compared with the CTL scheme (Fig. 5a). The average initial position errors for both schemes are near 30 km,

and the ME increases with increasing forecast time, generally in a consistent way, but the results are slightly better than the ACCESS-TC mean statistics (Davidson et al. 2014). The overall ME is 80 km for the CTL runs and 92 km for the SPY runs. These are not significant differences. The spray scheme makes clear improvements to the prediction of CP. As shown in Fig. 5b, both the MEs and root-mean-square errors (RMSEs) from the SPY tests are clearly reduced at almost all forecast times. The overall MEs and RMSEs are 13.8 and 20.5 hPa, respectively, for the CTL tests and 8.7 and 14.5 hPa for the SPY tests. This represents an improvement of 37% in ME and 29% in RMSE from the SPY runs in comparison with the CTL runs, with very small changes in the track forecasts. It is noted that for this limited sample large biases exist in the high intensities, which mainly occur in the shorter forecast times, and small biases exist in the weak intensities, which mainly occur in the longer forecast times. This leads to a decreasing error along the increasing forecast time shown in Fig. 5b.

Beyond a certain TC intensity, the improvement in CP predictions becomes evident with the spray inclusion scheme. The CP mean biases are plotted against the observed CPs in Fig. 6a. As we might expect, when CPs are lower than 955 hPa, MEs and RMSEs are clearly reduced in the SPY tests. When CPs are higher than 970 hPa, values of the MEs and RMSEs are very similar to their counterparts from the CTL tests. As discussed for the situation in Fig. 2a, the sea-spray-affected enthalpy exchange coefficient and declining drag coefficient only become active for wind speeds greater than approximately 20 and 30 m s⁻¹. This further demonstrates that the SPY scheme does not simply make stronger CP predictions. Improvement is also seen in the initialized TC circulations. As shown in Fig. 6b, the initial individual CPs for each run are also closer to the estimates using the spray scheme. For the control runs, the ME averaged over the initial pressures of all the forecasts is 17.6 hPa and the RMSE is 23.4 hPa. The values are reduced to 12.3 and 15.3 hPa, respectively, for the SPY runs, or 30% and 35% reductions from the CTL statistics. As described in section 3, ACCESS-TC employs the use of synthetic surface pressure observations

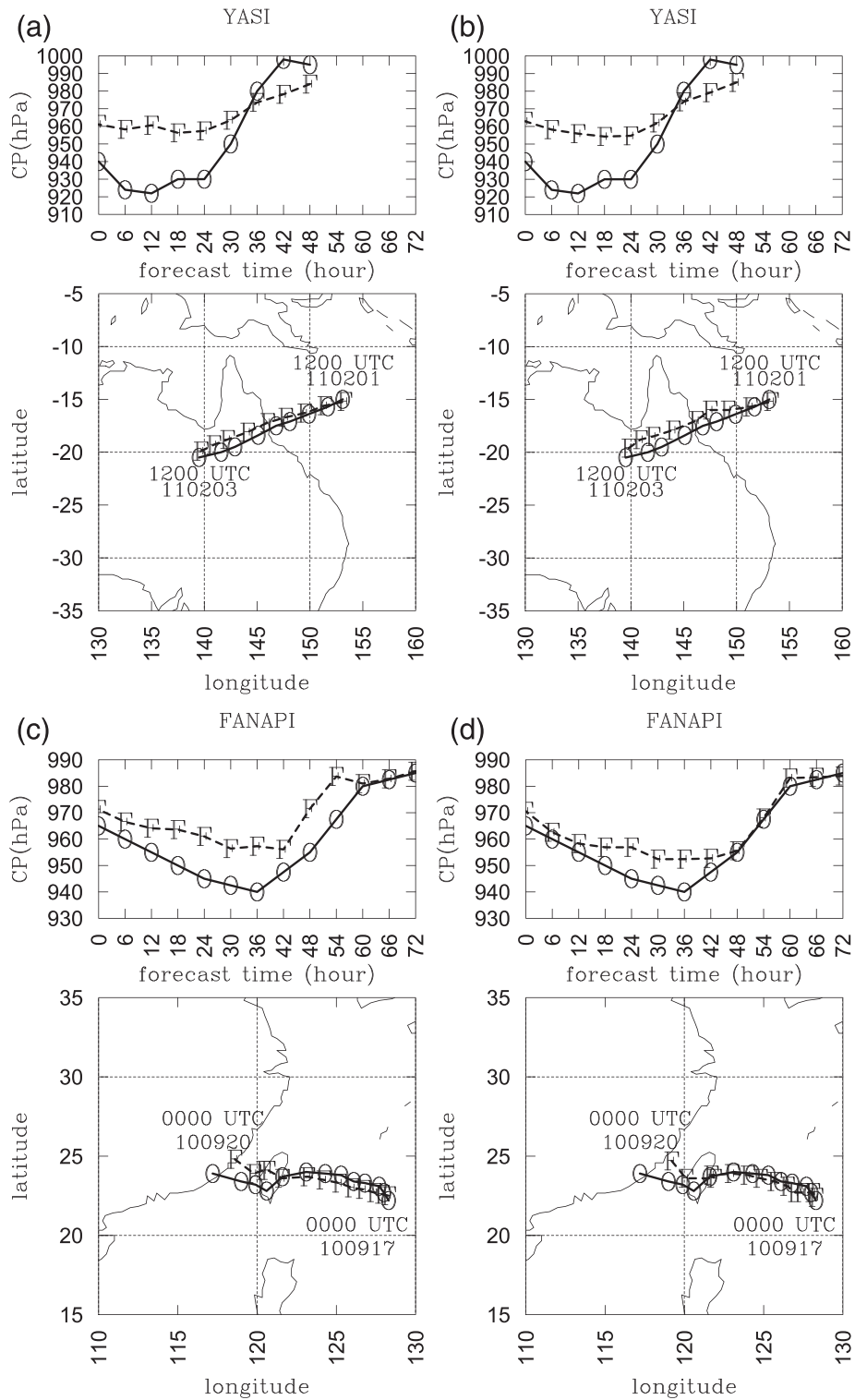


FIG. 3. Observed and 72-h forecast tracks and central pressures for TCs Yasi and Fanapi from (a),(c) CTL and (b),(d) SPY forecasts.

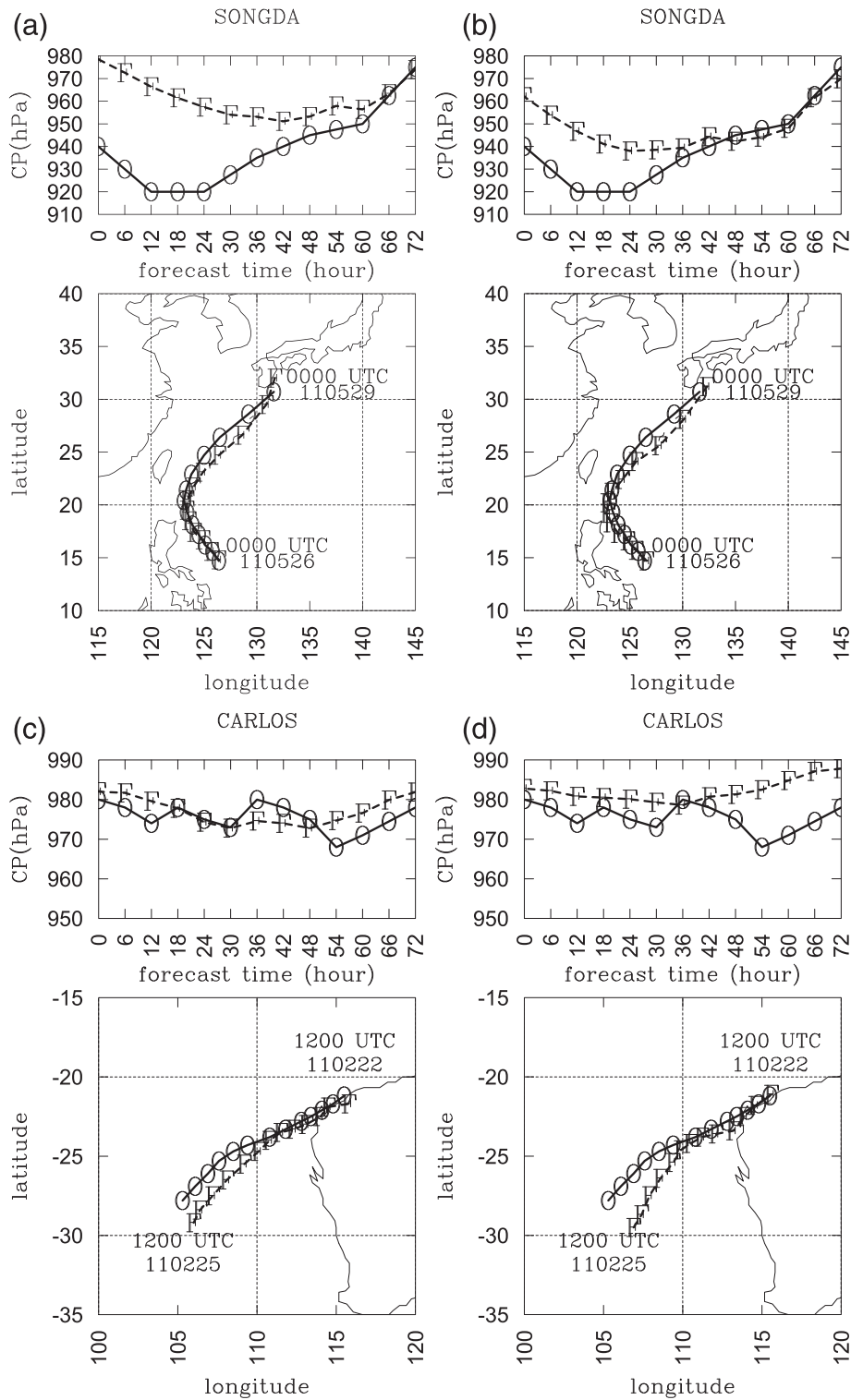


FIG. 4. Observed and 72-h forecast tracks and central pressures for TCs Songda and Carlos from (a),(c) CTL and (b),(d) SPY forecasts.

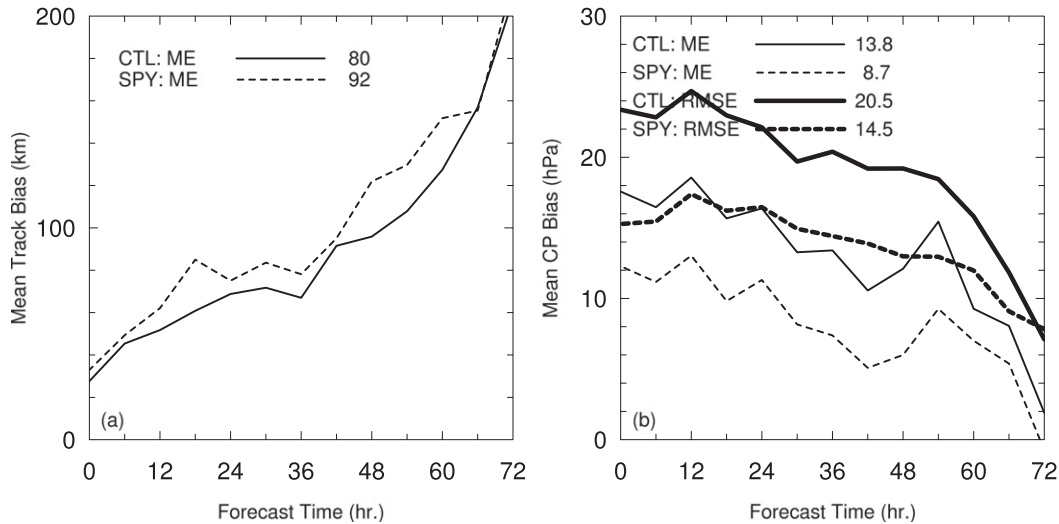


FIG. 5. Mean forecast biases against forecast time. (a) Mean track and (b) CP using CTL and SPY.

from a carefully constructed idealized vortex, and a five-cycle 4DVAR initialization to generate a TC structure (Davidson et al. 2014). This dynamic process also is affected by the changes in the surface exchanges induced by the parameterization changes, which has a positive influence on generating a better representation of the real structure.

The correlation between CP and the tangential wind maximum (VM) is generally summarized in the empirical relation of Dvorak (1975) over different ocean basins. Accordingly, corresponding to the improvement in CP predictions, comparison between the SPY and CTL tests shows clear increases in VMs obtained from the SPY tests for intensities greater than approximately 32 ms^{-1} . The increases are of the order of 8 ms^{-1} for

maximum winds of 50 ms^{-1} . This represents a 16% improvement from the SPY tests (Fig. 7).

b. Analysis of a rapid intensification case

To investigate the relationship between air–sea exchanges and the internal processes of TC intensity and structure changes, we choose TC Yasi (2011) as a detailed case study. We analyze the 72-h simulations for Yasi initialized at 1200 UTC 30 January 2011 with both the CTL and SPY configurations. Figure 8a shows the TC structure and intensity changes, which are represented by time series of CP, VM, the radius of the maximum wind (RMW), and the radii of the 64-, 50-, and 34-kt wind (R64, R50, and R34, respectively; $1 \text{ kt} = 0.51 \text{ m s}^{-1}$). The track forecast is also shown in

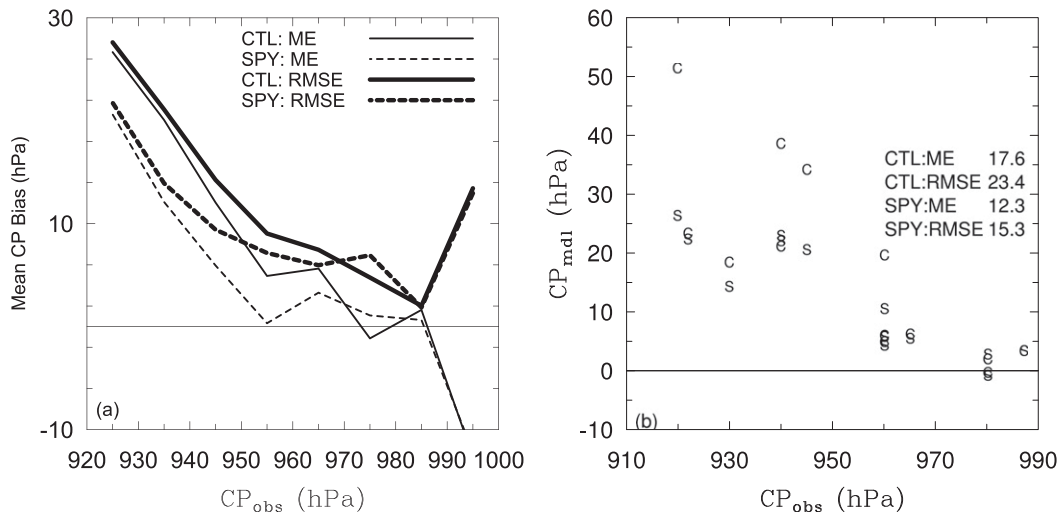


FIG. 6. (a) CP bias against observed CP. (b) Initial CP bias against observed CP.

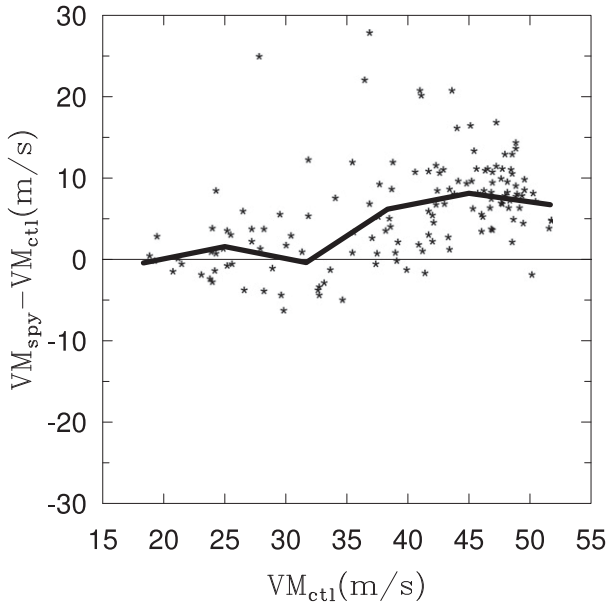


FIG. 7. Graph of VM_{CTL} vs $VM_{SPY} - VM_{CTL}$.

Figs. 8b and 8c. During the first 48 h, CP dips 33 hPa in the CTL test and 45 hPa in the SPY test. The latter represents the estimated pressure drop of 47 hPa more closely. The maximum wind increases during the forecast by roughly 20 m s^{-1} from the CTL test and 32 m s^{-1} from the SPY test. [Kaplan and DeMaria \(2003\)](#) define RI as a 24-h increase in the maximum sustained wind of 30 kt (15.4 m s^{-1}). RI has proven to be especially difficult for operational forecasting ([Elsberry et al. 2007](#)). The new

scheme has thus forecast the RI more satisfactorily. Also shown in [Fig. 8a](#) are the predicted TC size parameters from both schemes, represented here by R34, but also by R50 and R64. There is little difference in these parameters from the CTL and SPY forecasts. In addition, RMW is slightly smaller during most of the forecast with the SPY scheme, while the evolution is similar. Note that initially CP and VM values from both of the tests are quite similar. A relatively smaller inner-core structure develops from the SPY test, as indicated by the smaller RMW and R34. An inner-core contraction and TC intensification are clearly seen in the relation between VM and RMW. The TC size parameters, R34 from the two schemes, are basically the same, and so the TC size is almost unaffected by the new parameterization, even though the intensities are quite different. The forecast tracks from both the schemes are comparable with the observed curved track, which basically follows the environmental flow ([Figs. 8b and 8c](#)). As expected, the largest differences between the CTL and SPY experiments will be over the inner-core (approximately a radius of 100 km) where high wind speeds mean that the revised parameterizations will be active.

1) THE AIR-SEA SURFACE EXCHANGE COEFFICIENTS, SURFACE FLUXES, AND NEAR-SURFACE SIMULATIONS

We have derived azimuthally averaged coefficients of C_D and C_K from the model outputs to describe the difference between the two schemes. The coefficients are derived from the surface stress, sensible and latent heat

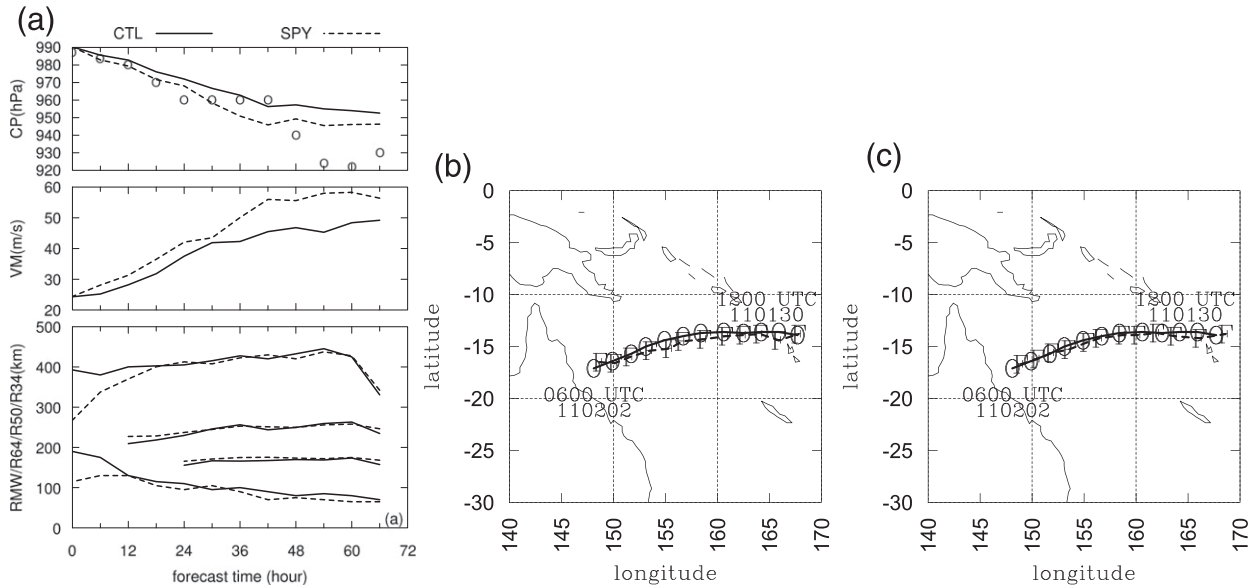


FIG. 8. RI case: (a) Time series of simulated CP, inner-core parameters of VM and RMW, and outer-ring wind radius R34, using CTL and SPY. The best-estimated CP is indicated with an open circle. (b),(c) Observed and 72-h forecast tracks from CTL and SPY, respectively.

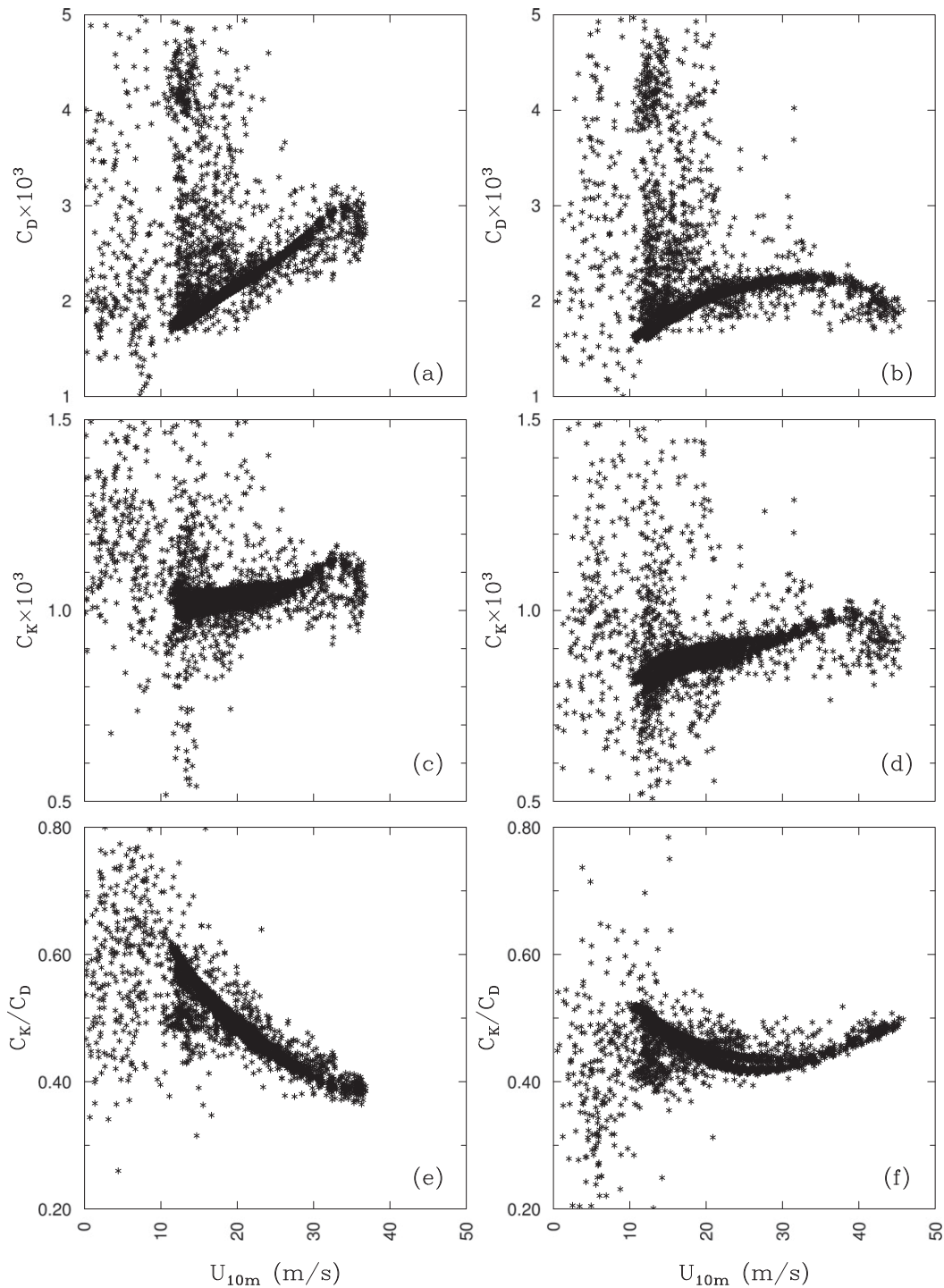


FIG. 9. Model-derived exchange coefficients and their ratios: (a),(b) C_D , (c),(d) C_K , and (e),(f) C_K/C_D , versus mean tangential wind at 10-m height. Shown are (left) CTL and (right) SPY surface exchange schemes.

fluxes, and the vertical gradient of the wind speed, temperature, and humidity. Detailed procedures are also referred to in the appendix of Bao et al. (2011). As shown in Fig. 9 from the 72-h forecast of the case, the

model-derived drag and enthalpy exchange coefficients generally preserve the patterns shown earlier in Fig. 2 for the theoretical formulation for a specific condition. As shown in Figs. 9a and 9b, when surface winds are

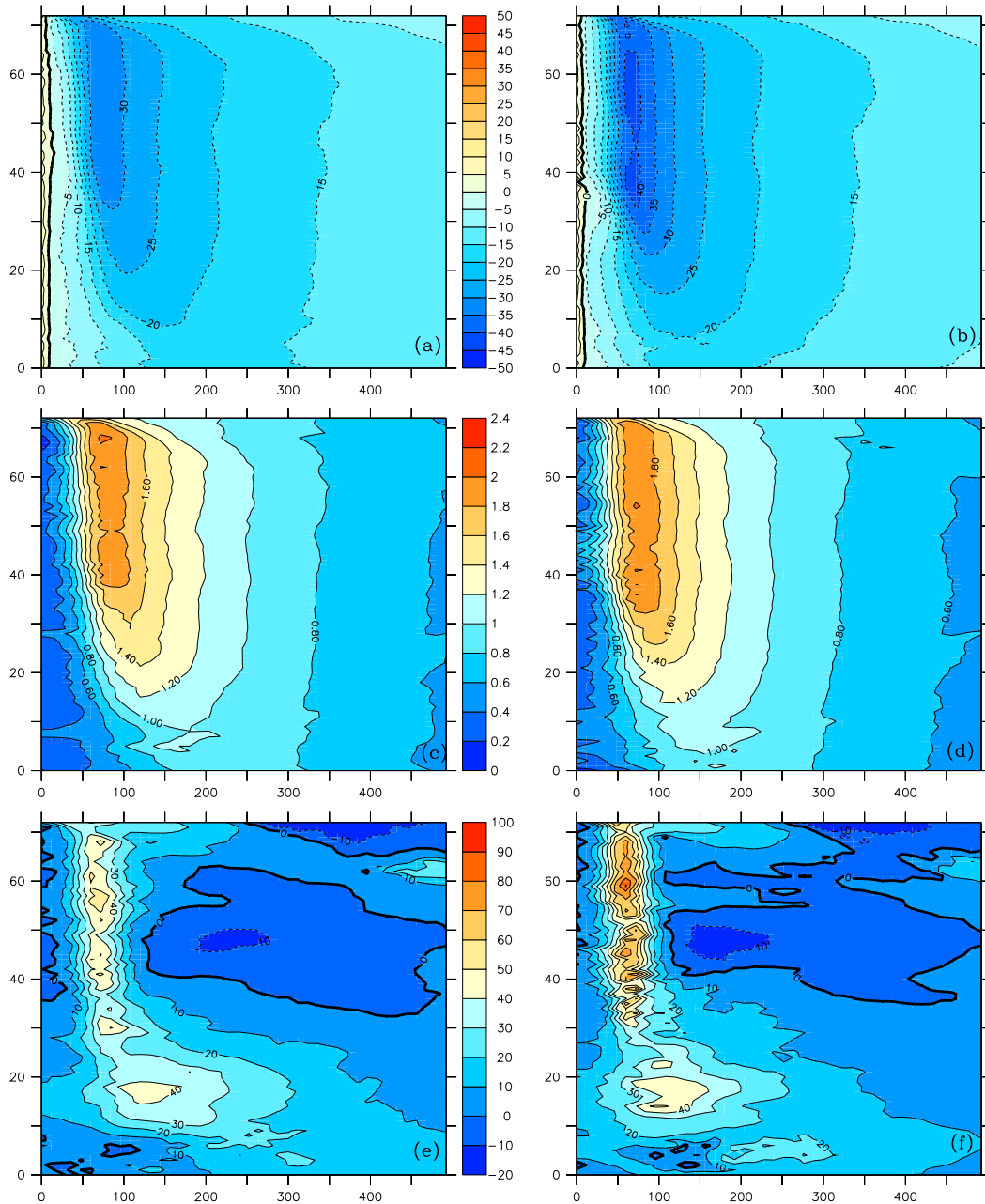


FIG. 10. Radius–time Hovmöller diagrams of azimuthal means of (a),(b) U_{10m} ($m s^{-1}$), (c),(d) U^* ($m s^{-1}$), (e),(f) SH ($W m^{-2}$), (g),(h) LH ($W m^{-2}$), (i),(j) enthalpy flux SH + LH ($W m^{-2}$), and (k),(l) SLP (hPa) for TC Yasi from base time 1800 UTC 30 Jan 2011. Shown for each pair are (left) CTL and (right) SPY runs.

under around $20 m s^{-1}$, C_D increases linearly with surface wind speed in both schemes. When the winds are greater than $20 m s^{-1}$, the drag coefficients for the two schemes begin to differ. The C_D results for the SPY test slightly increase with the increasing winds, level off around $35 m s^{-1}$, and then decrease with the stronger winds. The exchange coefficients for enthalpy fluxes for the SPY test are lower than those for the CTL test, and

both slightly increase with increasing winds. The ratios between C_K and C_D for the two schemes thus show different patterns. A nearly linearly decreasing trend between C_K/C_D is maintained with increasing winds for the CTL test, while such a trend becomes linearly increasing with increasing winds beyond $25 m s^{-1}$ for the SPY test. There is some sensitivity to the tangential wind calculation from the center-finding algorithm, especially

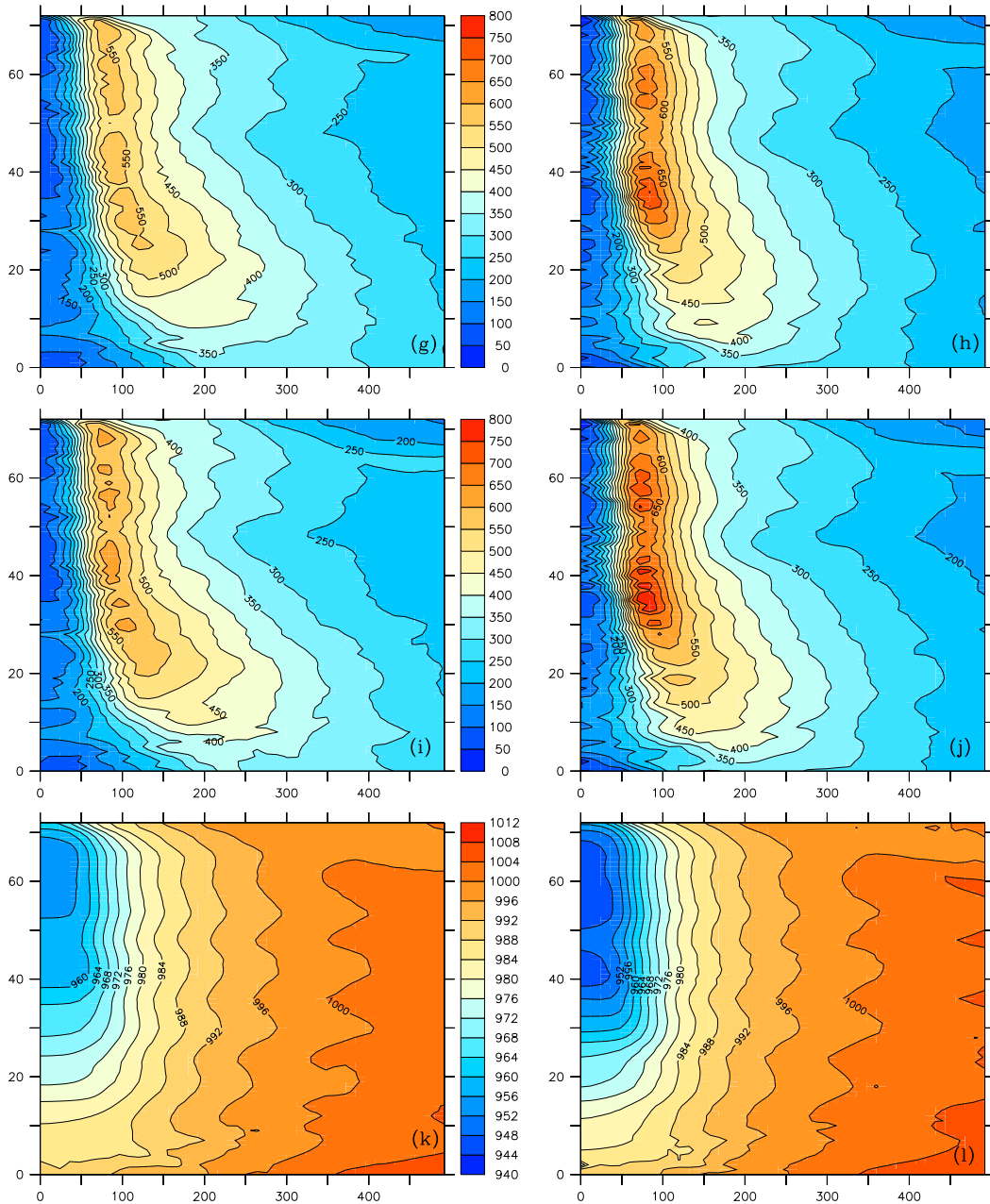


FIG. 10. (Continued)

for the low wind speeds. The large fluctuations in the coefficients and the ratios at winds below 20 m s^{-1} are due mainly to the uncertainty of the mean wind speed at these relatively low speeds.

Emanuel (1986, 1995) suggested a relationship between the maximum tangential wind speed averaged over the subcloud layer and the ratio of enthalpy to momentum exchange coefficients for a TC in quasi-equilibrium. As shown in his Fig. 1 (Emanuel 1995) the ratio increases nearly linearly with an increasing

maximum wind at high winds. With the SPY test, the ratio in Figs. 2b and 9f agrees quite well with Emanuel's theory.

Simulated surface variables and fluxes are displayed in pairs for the CTL and SPY tests in Fig. 10. Although the maximum 10-m tangential winds reach much higher values during the SPY test than during the CTL test (cf. Figs. 10a and 10b), the maximum surface friction velocities U^* for the SPY test do not show much higher values than the CTL (cf. Figs. 10c and 10d), given that at high winds a relatively low surface stress is achieved

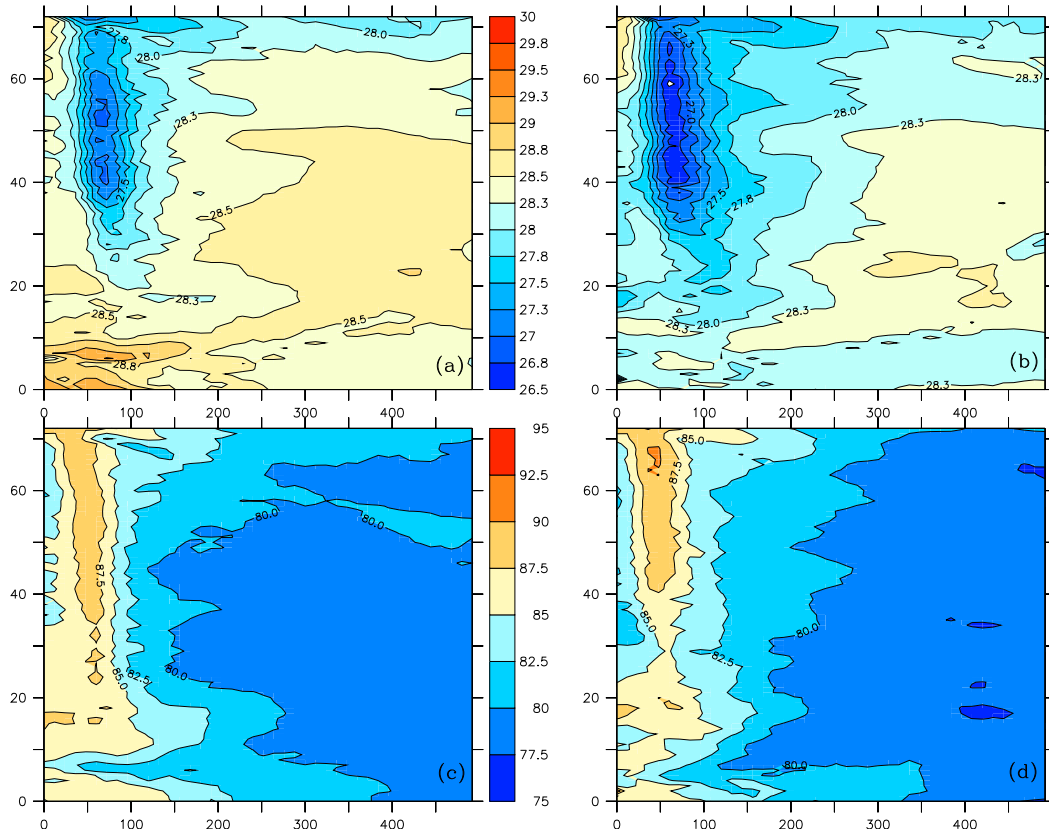


FIG. 11. Hovmöller diagrams of azimuthal means of near-surface model level (a),(b) temperature ($^{\circ}\text{C}$) and (c),(d) relative humidity (%) for TC Yasi from base time 1200 UTC 30 Jan 2011. Shown for each pair are (left) CTL and (right) SPY runs.

from the SPY scheme compared to that from the CTL scheme (Fig. 2c). That is, alternatively, for the same stress between the TC atmosphere and the water surface, higher winds are simulated with the new scheme. A somewhat broad region of sensible and latent heat fluxes occurs in the CTL run, especially prior to the intensification process ($t < 30$ h) (cf. Figs. 10e and 10f, as well as Figs. 10f, 10g, and 10h). The sensible heat flux is higher in the SPY run than the CTL run with its maximum between 55 and 60 h for both the runs (Figs. 10e,f). We note that the sensible heat flux is still higher in SPY than CTL. This is mainly because of the effect of larger surface winds in SPY than CTL. The latent heat flux is higher and occurs earlier with the maximum in the SPY run than the CTL run (Figs. 10g,h). Their sum, the time evolution of the enthalpy flux (cf. Figs. 10i and 10j), resembles that of the latent heat flux as it is the major contributor to the enthalpy flux. It is noted that there are clearly two enthalpy flux maxima from the SPY tests (Fig. 10j) between 30 and 40 h, and between 55 and 60 h, that correspond to the two sea level pressure minima in the TC eye (Fig. 10l). For CTL, there are a series of enthalpy flux maxima (Fig. 10i) and no clear dual surface

level pressure (SLP) minima at the simulated center (Fig. 10k). These dual peaks are also represented in the surface wind for the SPY run (Fig. 10b). Two such CP minima during the TC evolution are also seen in the observations around 24 and 60 h (Fig. 8a), although the timings are biased between the SPY simulations and the observations. This finding suggests that the TC underwent two cycles of intensification over the ocean during the simulation time, and that the SPY run, with the revised air-sea exchange scheme, better captures the two cycles. The near-surface meteorological fields and their evolution are thus changed with the revised scheme in a way that seems more consistent with the observed TC intensity change.

We also plot the near-surface temperature and specific humidity in Fig. 11. Compared with the CTL test, a relatively cold and dry core is initialized with the SPY test, which consistently increases its temperature and humidity during the forecast hours, while the former roughly retains its temperature and humidity (Figs. 11a,b and Figs. 11c,d, respectively). There is still some cooling for the near-surface air, although it is not as strong as in the

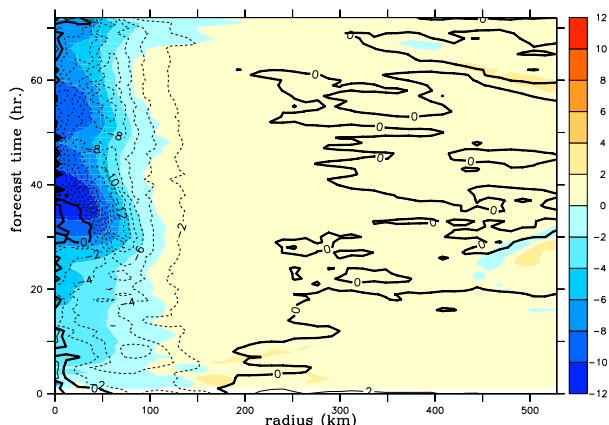


FIG. 12. Radius-time cross section of SLP (hPa) difference (shaded) and the near-surface tangential wind (black contours) between the CTL and SPY tests.

inner core, because the revised parameterization has only a weak effect at low winds.

2) IMPACT ON TC INNER-CORE (EYE AND EYEWALL) STRUCTURE CHANGE

Although the pressure drop between the eye center and eyewall accounts for less than half of the drop between the eye center and the environment (Willoughby 1998), the difference in SLP falls between the two tests during the RI occurs mainly in the vicinity of the TC eye and near the eyewall. As shown in Fig. 12 (shading), the differences mainly occur within a radius of 100 km of the center. The difference reaches 10 hPa in the center during the time between 30 and 60 h. Outside the radius of 100 km, the

difference is within 2 hPa. Correspondingly, as shown by the contours in Fig. 12, the difference in the surface tangential winds also occurs mostly within a radius of 100 km of the center. The differences are around or more than 20 m s^{-1} near the eyewall during the time between 30 and 60 h. Outside the radius of 100 km, the difference is within 2 m s^{-1} .

Figure 13 shows radius-time sections of tropospheric-mean (averaged over 0–18 km) vertical motion $\bar{w}_{0-18\text{km}}$ for CTL and SPY. In conjunction with the 10-m tangential wind U_{10} (Figs. 10a,b) and the azimuthal-mean SLP (Figs. 10k,l), the patterns of intensification and structure are similar in CTL and SPY, suggesting that the modifications and additions to the parameterizations are working in a way that is consistent with the earlier formulation. The SLP and U_{10} diagrams show the intensification in SPY is stronger, occurs earlier, and develops much more rapidly. The largest changes occur from about 20 to 48 h, which corresponds with the period of rapid intensification illustrated in Fig. 8 and the sharp increase in surface fluxes, shown in Fig. 10. Almost all of the changes and differences from the CTL experiment occur within 100 km of the circulation center. This is the region where we expect the reduced drag and the sea spray parameterization at high wind speeds to have the largest effect. Note however that differences are also evident to very small radii in the eye where wind speeds are very low. We suggest that the changes in surface fluxes from the revised parameterizations over high-wind regions mostly under the eyewall provoke 1) the consequent changes in convective activity in the eyewall

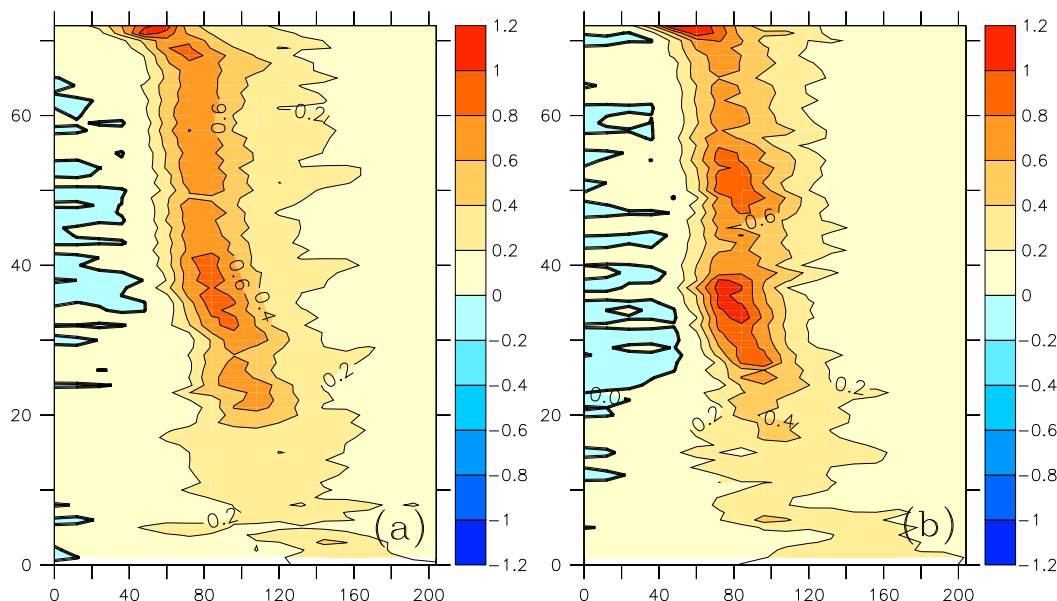


FIG. 13. Radius-time section of $\bar{w}_{0-18\text{km}}$ (m s^{-1}) for (a) CTL and (b) SPY.

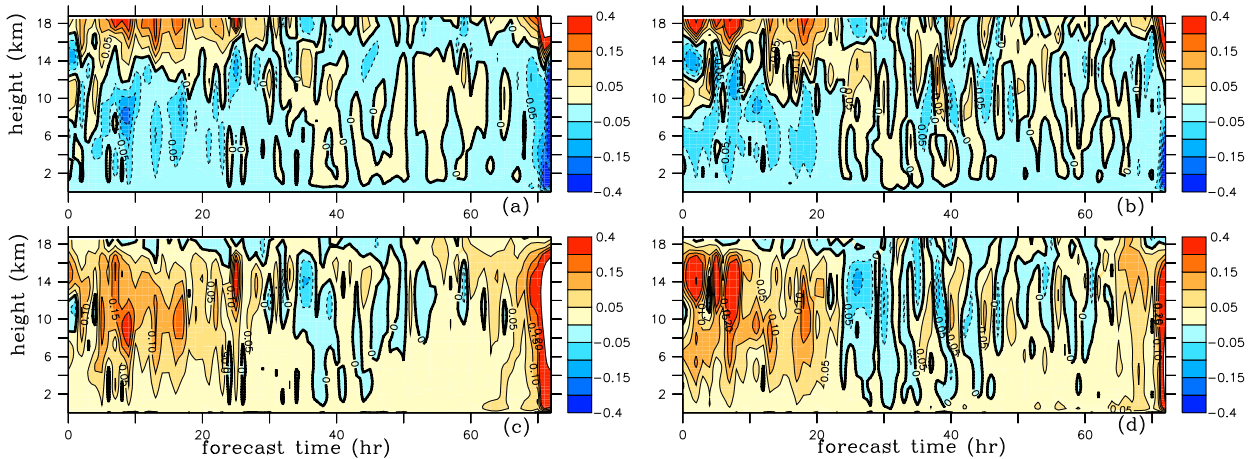


FIG. 14. Cancellation of contributors to the divergence in the TC eye from (a),(b) the radial wind and (c),(d) vertical motion for (left) CTL and (right) SPY in Eq. (10b). The units are m s^{-1} .

and 2) changes in the dynamics of the intensification and characteristics of the eye. Note that, as indicated above, there are small differences in the location of the radius of maximum eyewall convection but the intensity of $\bar{w}_{0-18\text{km}}$ in the eye and the eyewall is much stronger in the SPY run. There appear to be short-term fluctuations in the radius of the azimuthal-mean eyewall, as indicated by the changes in the location of the $\bar{w}_{0-18\text{km}} = 0$ line in Figs. 13c and 13f. In addition, there seems also to be some relationship between fluctuations in the eyewall radius and changes in the ascent field within the eye. In fact, this suggests a radial pulsating of the eye and eyewall convection on relatively short time scales. Further diagnostics are needed to understand this phenomenon. However, we suggest it may be linked to eyewall convective bursts, with the eyewall convection exhausting the convective available potential energy (CAPE; Nguyen et al. 2011), and then relaxing as the CAPE is replenished by the surface heat fluxes, which in SPY have been enhanced via reduced drag and the sea spray effects. We note that the pulsation in ascent in the eyewall and descent in the eye appear to be linked and out of phase, and the radial and temporal pulsations may be important for the critical subsidence in the eye. We can also investigate such pulsations through the continuity constraint, which is expressed as follows in cylindrical coordinates under an axisymmetric assumption:

$$\frac{1}{\rho} \frac{d\rho}{dt} + \left[\frac{1}{r} \frac{\partial}{\partial r} (ru) + \frac{\partial w}{\partial z} \right] = 0, \quad (10a)$$

where ρ denotes the air density, r the radius, z the height, u the radial velocity, and w the vertical velocity. When integrated over the height from the surface to a certain

level z and over the TC radius from the center to a certain distance, the normalized divergence term can be expressed as

$$\begin{aligned} & \frac{2}{r^2} \int_0^r \int_0^z \left[\frac{1}{r'} \frac{\partial}{\partial r'} (r'u) + \frac{\partial w}{\partial z'} \right] dz' dr' \\ &= \frac{2}{r} \int_0^z u(r, z') dz' + \frac{2}{r^2} \int_0^r rw(r', z) dr', \end{aligned} \quad (10b)$$

where the prime denotes the variables to be integrated. The equation shows that the divergence is composed of contributions from radial and vertical motions. As shown in Fig. 14a, within the eye ($r < 42$ km), the two terms cancel each other at most times in the eye where the air density change is relatively small as no water vapor phase changes occur. There are strong correlations between the pulsations of radial wind and vertical motion. This further demonstrates that the temporal pulsations of the radial motion are important for the critical subsidence in the eye. We suggest that there is a strong correlation between these dynamical features in the forecasts and the surface fluxes, which are of course dependent on the surface flux parameterizations.

We investigate the inner-core thermal and kinetic changes during the simulated RI of Yasi with control and spray scheme tests. Fig. 15 displays the evolution of vertical structures of thermal and dynamical variables. The model does not simulate a clear inversion layer, as indicated in Willoughby (1998). There are high vertical gradients in potential temperature θ around 6–7 km during the forecast RI (Figs. 15a,b), which could be contributed to by large condensational heating at that height (Figs. 15e,f). A major distinguishing feature between the CTL and SPY forecasts is that strong subsidence occurs earlier in the eye during RI from the SPY

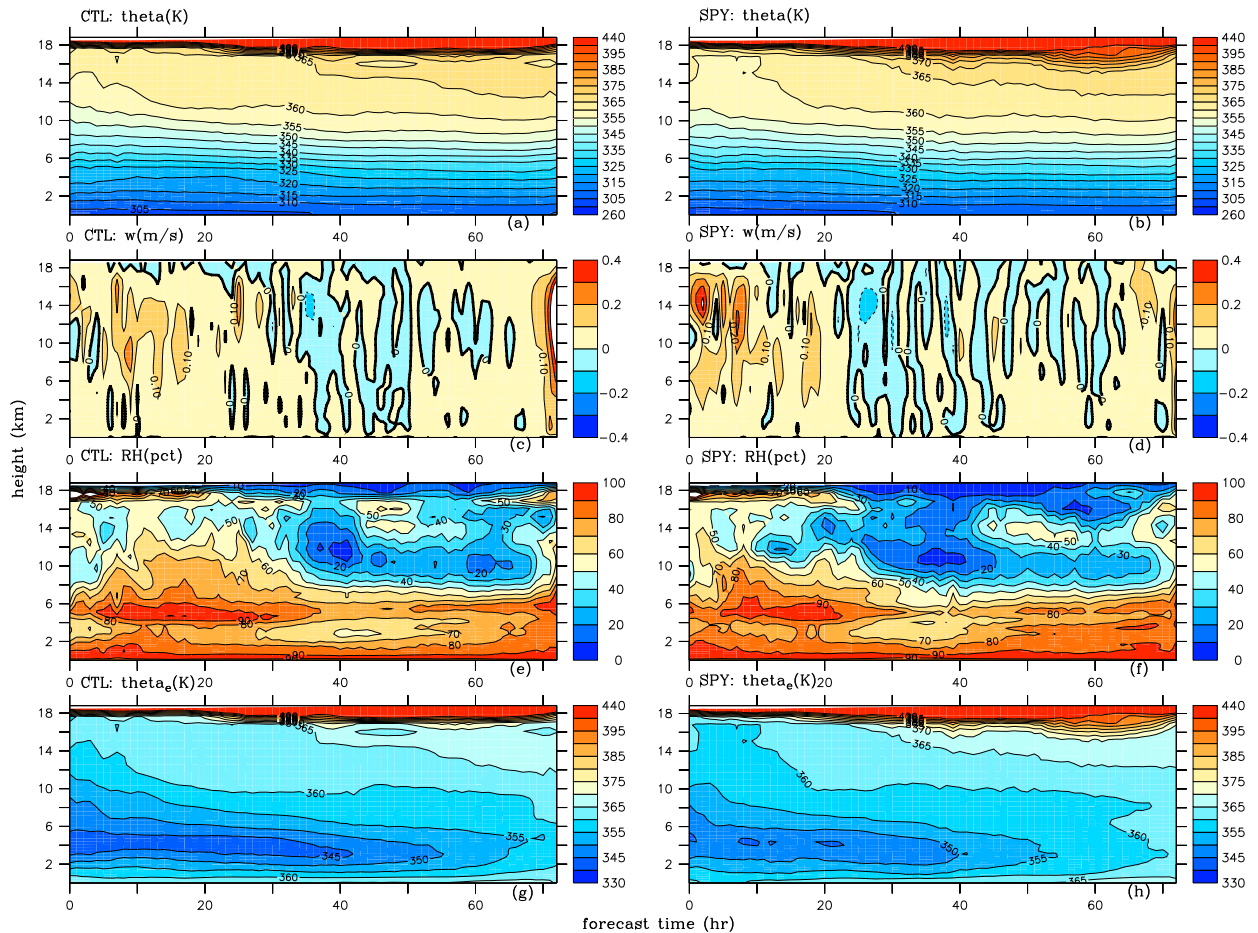


FIG. 15. Time–height cross sections of (a),(b) θ (K), (c),(d) w (m s^{-1}), (e),(f) RH (%), and (g),(h) θ_e (K) in the TC eye with the CTL and SPY tests.

forecast (Figs. 15c,d). Below 4 km, both of the tests predict a moist layer (RH > 90%) roughly below 1 km while a dry layer (RH < 80%) is approximately centered at 2.5 km. Between these two experiments, the SPY test predicts a thicker moist layer and a relatively less dry upper layer compared to CTL. Subsidence of air aloft is believed to be the source of the warming and drying of the eye air (Willoughby 1998). In the TC eye, an initially less stable stratification in the layer between about 10 and 16 km is seen in the SPY test (cf. Figs. 15b and 15a). This may allow less inhibition to earlier subsidence between 20 and 40 h in the SPY test while it is at 30–50 h in the CTL test (cf. Figs. 15d and 15c). Consequentially, dry air (RH < 50%) begins to dominate the upper layer (>10 km) during earlier simulation times (Figs. 15e,d,f). Both of the tests show that pseudoequivalent potential temperature θ_e decreases, then increases with height, and reaches a minimum at around 4 km (Figs. 15g,h). Compared with the CTL result, the SPY test predicts weaker vertical gradients of θ_e , due to the relatively high

moisture in the low atmosphere. That is, conditional instability is still present but weaker in the SPY run, possibly because of the more active convection creating a more stable environment.

In the eye and eyewall region, the new parameterization of the surface exchange leads to some changes to the thermal structure in the low atmosphere. Figure 16 shows the time evolution of the thermal structure in the low atmosphere (<2.5 km). Compared with the CTL results, the SPY test shows a slightly cooler and moister lower layer (Figs. 16a,b and 16c,d). This is also discussed in Wang et al. (2001), who indicate that some observational evidence may support the real existence of the phenomena (Cione et al. 2000). Both of the tests exhibit a shallow mixing layer (<300 m) near the surface that is defined by a near-constant potential temperature and unsaturated layer (RH < 90%) (Figs. 16c, d and 16e,f). This structure seems consistent with the observational studies of Willoughby (1998) and Barnes and Fuentes (2010).

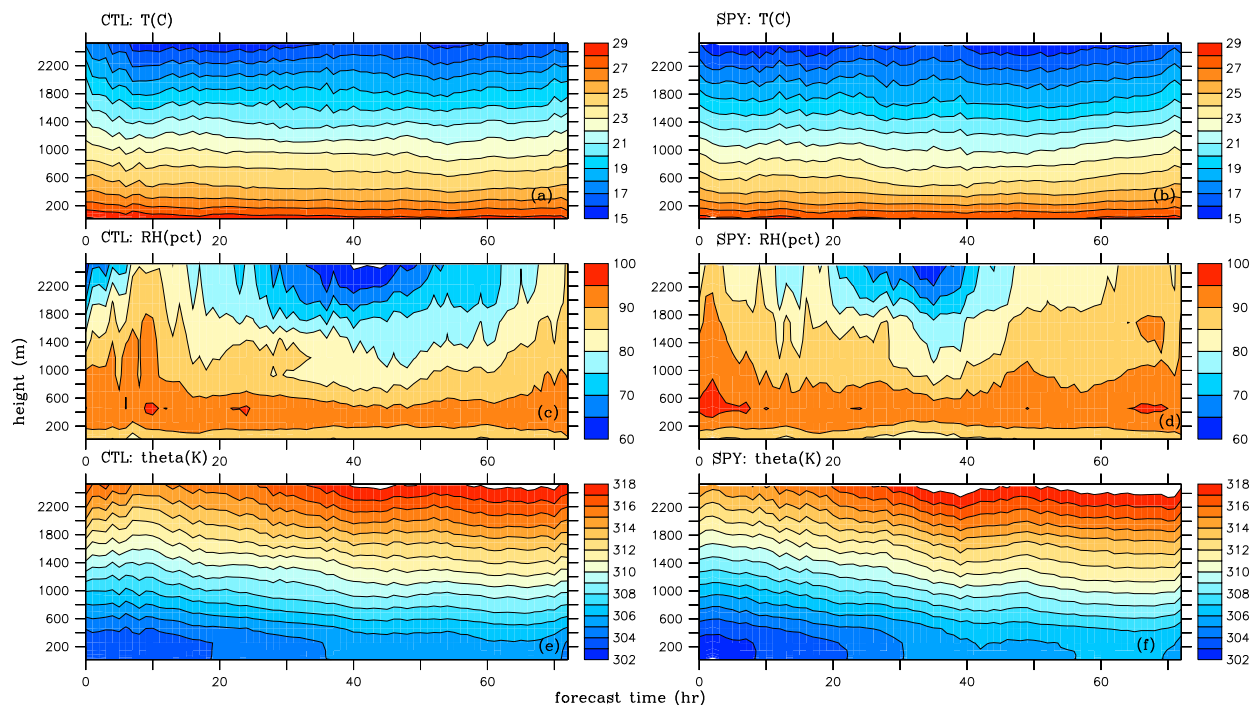


FIG. 16. Time–height cross sections in the lower atmosphere of (a),(b) T ($^{\circ}\text{C}$), (c),(d) RH (%), and (e),(f) θ (K) in the TC eye with the CTL and SPY tests.

Theoretical and observational evidence (e.g., Rogers et al. 2013; Vigh and Schubert 2009; Schubert and Hack 1982) suggests that during intensification convection is located on the inside of R_{\max} , defined as radius of maximum azimuthal-mean tangential wind, where the inertial stability is high and convective heating can act efficiently to create the surface pressure fall. The overlap between regions of ascent and large inertial stability $\{I^2 = [(v/r) + (\partial v/\partial r) + f][2(v/r) + f]\}$, where v is the tangential wind and f the Coriolis parameter; e.g., Schubert and Hack (1982)} provides a favorable situation for TC intensification. Also, during TC intensification, a radial convergence maximum is located within the R_{\max} and within the TC boundary layer. As argued in Montgomery et al. (2014), and Smith et al. (2009), this maximum is due to the convergence of absolute angular momentum exceeding the frictional torque from the ocean surface, providing a possible forcing for ascending flow within R_{\max} . In Figs. 17 and 18a–d we show I^2 and divergence around 36 h (averaged between 34 and 38 h) when CTL simulates a low intensification rate and SPY forecasts a high intensification rate, and around 60-h when CTL continuously simulates a low intensification rate while SPY forecasts a nearly steady state. As shown in Figs. 17a, 17b, 18a, and 18b, both I^2 and the vertical motion are located inside of the R_{\max} , and are collocated especially in the lower atmosphere, except in Fig. 18b. In Fig. 18b, for

the nearly steady state of the SPY forecast around 60 h, I^2 is located more inside of the vertical motion. The I^2 result from SPY is much larger than that from CTL, while the vertical motions are slightly higher in SPY than in the CTL test. As shown in Figs. 17c, 17d, 18c, and 18d, the convergence coincides quite well with the agradient wind, defined as the tangential wind minus the gradient wind in both runs. Note that in cylindrical coordinates a cyclonic tangential or gradient wind is negative in the Southern Hemisphere, which means a supergradient wind is negative. The convergence centers are notably located within their corresponding R_{\max} when CTL and SPY simulate intensification, as shown in Figs. 17c, 17d, and 18c. The convergence center mostly coincides with the R_{\max} when SPY simulates a nearly steady state, as shown in Fig. 18d. Near the surface, subgradient winds occur with both of the tests. As shown in Figs. 17e, 17f, 18e, and 18f in both of the tests at 36- and 60-h forecast times, the eye seems to serve as a reservoir of equivalent potential temperature θ_e with its maximum near the surface during the simulated intensification stage as well as for the nearly steady-state phase. As discussed earlier, studies have shown high θ_e in the eye could be favored (Barnes and Fuentes 2010; Miyamoto and Takemi 2013) or not play a role (Bryan and Rotunno 2009; Wang and Xu 2010) during RI. From the current study the role of the θ_e reservoir for RI seems to not be crucial. The θ_e

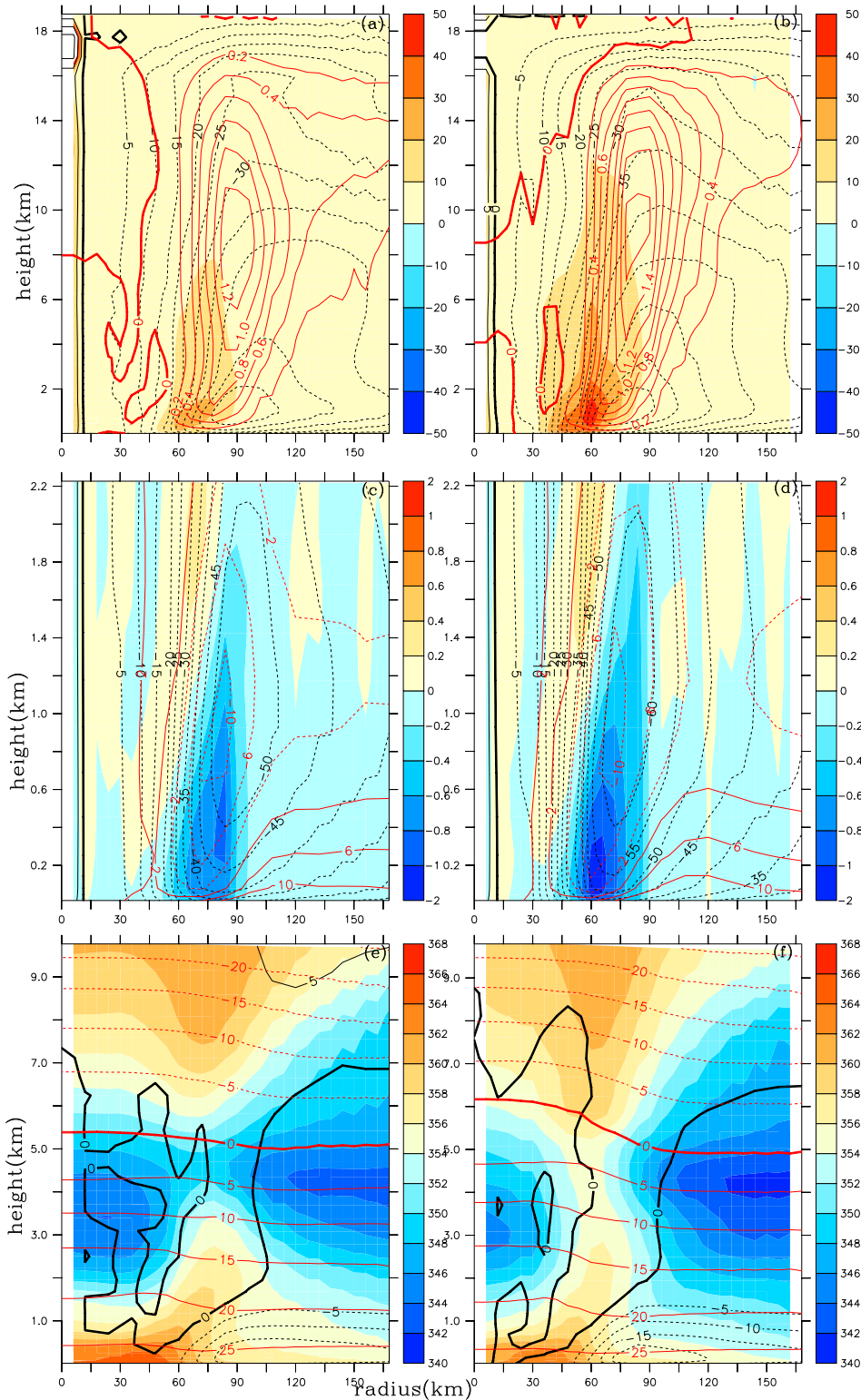


FIG. 17. Radius–height azimuthal mean fields at 36 h: (top) P^2 (shaded; $\times 10^{-7} \text{ s}^{-2}$), tangential wind (black contours; m s^{-1}) and w (red contour; m s^{-1}); (middle) divergence (shaded; $\times 10^{-3} \text{ s}^{-1}$), tangential wind (black contours; m s^{-1}), and gradient wind (red contours; m s^{-1}); and (bottom) θ_e (shaded; K), radial wind (black contours; m s^{-1}), and T (red contours; $^{\circ}\text{C}$) for (a),(c),(d) CTL and (b),(e),(f) SPY tests.

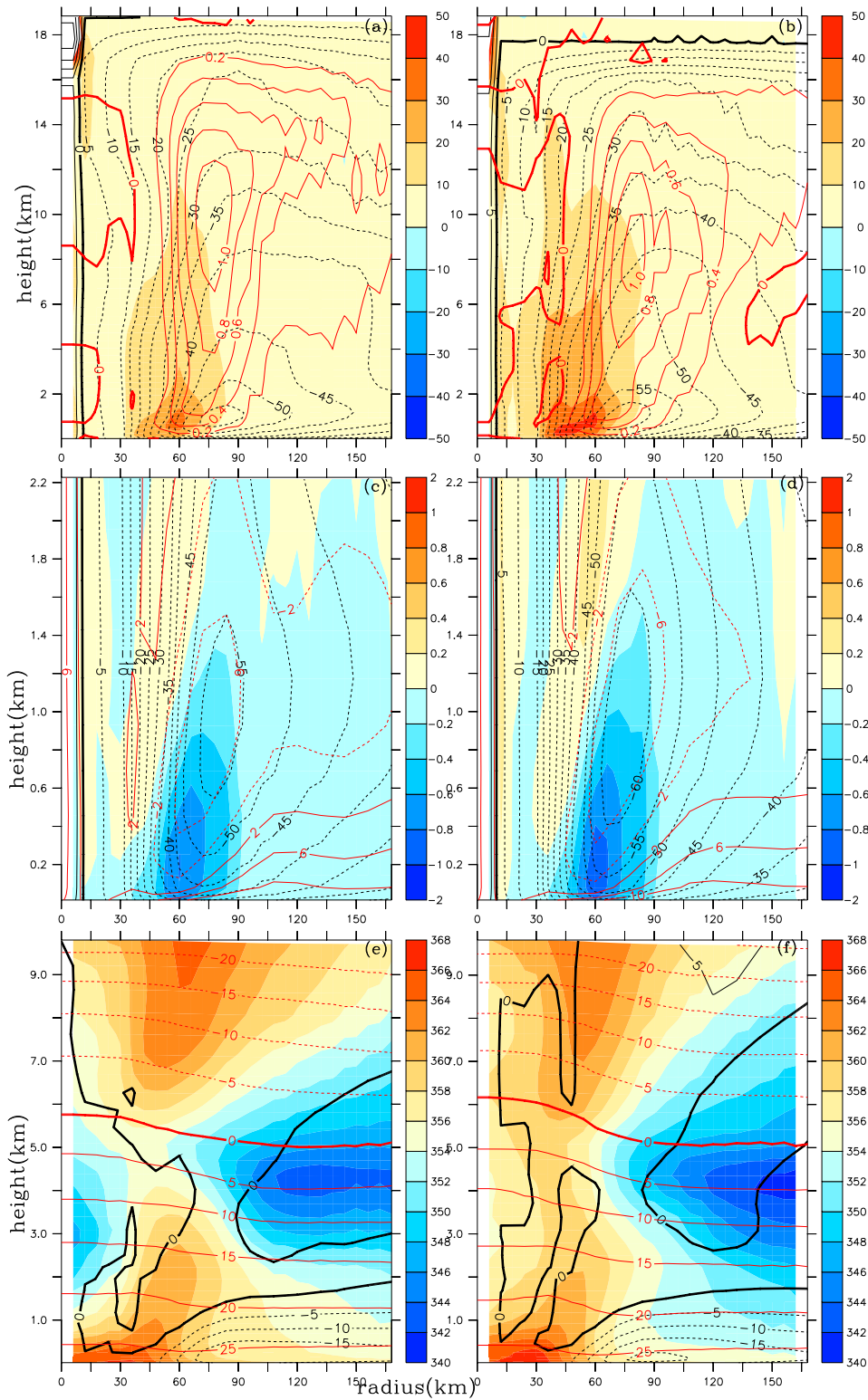


FIG. 18. As in Fig. 17, but the radius–height azimuthal-mean fields at 60 h.

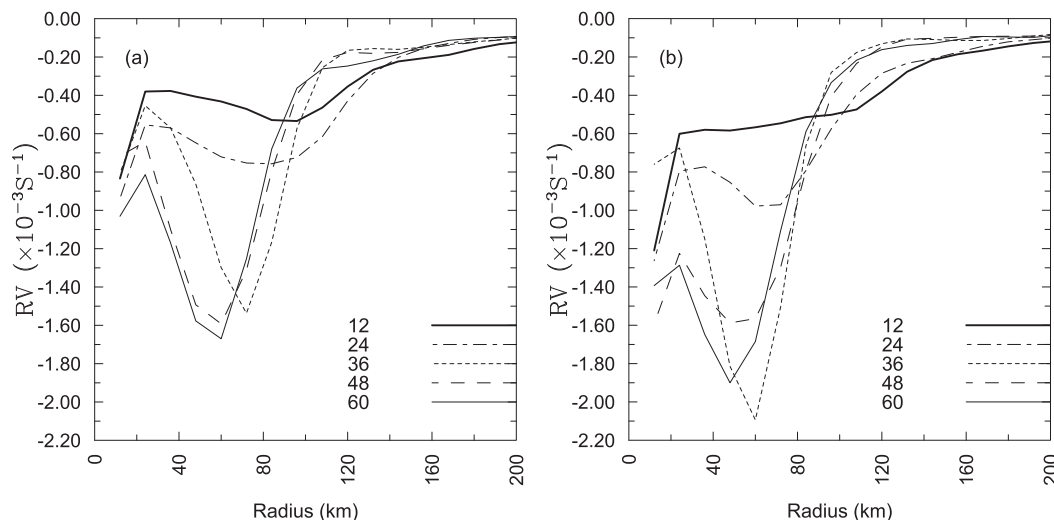


FIG. 19. Radial distributions of RV (10^{-3} s^{-1}) around 2-km height for the (a) CTL and (b) SPY tests at different forecast hours.

maximum is consistent with the radial wind field for both of the tests, implying that it is the radial wind field that accumulates the high θ_e in the core. This is not confined by the mixing layer depth but seems to be determined by the inflow field of the secondary circulation. A distinguishing feature of the θ_e vertical distribution for the simulated steady state is that a warmer center overlays the warm surface θ_e (cf. Figs. 18e and 17e, 17f, and 18e), since the circulation has already rapidly intensified and the central pressure is low. Although the SPY test shows a higher intensification rate at 36 h than the CTL test, the θ_e maximum is weaker in the SPY than the CTL test, because of cooler temperatures in the low levels in the SPY test. While at 60 h, the higher θ_e maximum in the SPY test than the CTL test is due to moister air at low levels in the SPY test. It seems that while the convection is more active in the SPY runs, it consumes CAPE and reduces boundary layer θ_e , resulting in lower values of these quantities during RI. This is similar to the results found by Nguyen et al. (2011).

Studies show that notable differences in the radial profile of relative vorticity (RV) exist between storms undergoing RI and storms that are steady state (SS). Rogers et al. (2013), from a statistical survey of airborne Doppler observations of TCs, conclude that there is a ringlike structure for RI with maximum magnitude of RV within R_{max} between $0.3 R_{\text{max}}$ and $0.6 R_{\text{max}}$, while for SS such maxima are much closer to the eye center with higher RV in the eye (their Fig. 4b). Nguyen et al. (2011), from a numerical study, described a similar dual appearance of a monopole structure with maximum vorticity near the center of the circulation, and a ringlike structure with maximum vorticity at some radius from

the center. Other studies also show that the differences in RV profiles are closely related to the TC development status (e.g., Kossin and Eastin 2001). Such differences in the RV profiles are also notable from our simulations between the CTL and SPY tests. As shown in Fig. 19, for SPY, during the early hours the maximum vorticity is located at the center of the circulation (monopole structure) and is evolving toward a ringlike structure. As RI further develops, a strong ringlike RV structure occurs by 36 h. RV then becomes weaker near the eyewall and stronger near the eye center when the simulated TC becomes nearly steady (the lines on 48 and 60 h, respectively). For CTL, a slow but steady intensification in the later hours (36, 48, and 60 h) maintains the ringlike RV profiles.

The above results suggest that both reduced drag and a sea spray parameterization may be needed to simulate TC intensification, consistent with previous studies (e.g., Nguyen et al. 2011; Kossin and Eastin 2001; Montgomery et al. 2014; Smith et al. 2009). The revised scheme appears to simulate these processes better and also better represents the evolution to a steady-state TC.

3) ANALYSIS OF RAPID INTENSIFICATION BASED ON THE MPI FRAMEWORK

Based on the earlier discussion, we can now discuss the thermodynamic processes within the frame work of Emanuel’s hurricane maximum potential intensity (MPI) theory. Viewing a hurricane as a heat/Carnot engine, Emanuel (1986, 1995, 1997) assumed that in an equilibrium state when the hurricane reaches its MPI, the entropy added to the atmosphere from the ocean is balanced by the surface friction dissipation from the

atmosphere to the ocean over radii between the radius of the eyewall r_m and an outer radius r_0 :

$$\int_{r_m}^{r_0} \rho \varepsilon T_s C_K |V| (s_{s^*} - s_b) r dr = \int_{r_m}^{r_0} \rho C_D |V|^3 r dr. \quad (11a)$$

In addition to the variables previously defined, V is the near-surface layer wind speed, T_s is the sea surface temperature, s_{s^*} is the saturation entropy of the ocean surface, s_b is the entropy of the subcloud-layer air, and ε is the thermodynamic efficiency of the heat engine that has $\varepsilon = (T_s - T_t)/T_t$ (Bister and Emanuel 1998). Meanwhile, T_t is the mean tropospheric outflow temperature. The theory further assumes that the largest contributions to the integrals on both sides of Eq. (11a) arise from the radius around r_m , which is approximately RMW. Given $s = c_p \ln \theta$, Emanuel further showed that the potential maximum gradient wind speed is (<http://wind.mit.edu/~emanuel/pcmin/pclat/pclat.html>)

$$V_{\text{MPI},1} = \sqrt{c_p T_s \frac{T_s - T_t}{T_t} \left[\frac{C_K}{C_D} (\ln \theta_{e,s^*} - \ln \theta_{e,b}) \right] \Bigg|_{\text{RMW}}}, \quad (11b)$$

where c_p is the heat capacity at constant pressure, θ_{e,s^*} is the saturation equivalent potential temperature at the sea surface, and $\theta_{e,b}$ is the boundary layer equivalent potential temperature. The terms C_K , C_D , θ_{e,s^*} , and $\theta_{e,b}$ are evaluated at RMW. The speed can also be expressed in terms of CAPE, given the relation between CAPE and entropy (Emanuel 1994, Eq. 6.4.2):

$$V_{\text{MPI},2} = \sqrt{\frac{T_s}{T_t} \left[\frac{C_K}{C_D} (\text{CAPE}_s - \text{CAPE}_b) \right] \Bigg|_{\text{RMW}}}, \quad (11c)$$

where CAPE_s is CAPE computed using an air parcel lifted from saturation at the sea level and CAPE_b is that of the boundary layer air. Both CAPE_s and CAPE_b are also evaluated at the RMW. We use Eqs. (11b) and (11c) to investigate the relation between the MPI wind speed and the model-simulated maximum winds, as well as other thermodynamic properties, especially the two CAPEs and C_K/C_D , with the aim of understanding more precisely the impact of the improved parameterizations on the rapid intensification.

We calculated CAPE, V_{MPI} , and the components of V_{MPI} and illustrate them in Fig. 20. As shown in Fig. 20a, both the $V_{\text{MPI},1}$ and $V_{\text{MPI},2}$ results are quite similar, and the maximum boundary layer-averaged tangential winds $V_{m,B}$ from both the CTL and SPY tests

start to intensify at the beginning of the model simulations and maintain a similar pace until hour 24, when V_{MPI} results for both of the tests are much larger than their corresponding $V_{m,B}$ results. During the period, both $V_{m,B}$ and V_{MPI} in the SPY test are consistently larger than their counterparts in the CTL test. After hour 24, the difference between the SPY and CTL V_{MPI} values becomes large, as does $V_{m,B}$, until around hour 39, when both V_{MPI} and $V_{m,B}$ start to become steady. After hour 39, when $V_{m,B}$ reaches steady state, the difference between V_{MPI} and $V_{m,B}$ becomes smaller, yet V_{MPI} is still larger than $V_{m,B}$ for both of the tests. The matches between MPI and numerical simulations have been studied by Wang and Xu (2010). The above description suggests, but does not demonstrate, that the MPI tangential wind guides and bounds the model-simulated tangential wind from its rapid intensification to its steady state.

We decompose the components in Eqs. (11b) and (11c) to investigate their contributions to V_{MPI} . We plot C_K/C_D , T_t and T_s , θ_{e,s^*} and $\theta_{e,b}$, and CAPE_s and CAPE_b in Figs. 20b–e, as well as the ratio of each component of $T_s[(T_s - T_t)/T_t]$, C_K/C_D , $\ln \theta_{e,s^*} - \ln \theta_{e,b}$, and $\text{CAPE}_s - \text{CAPE}_b$, from the SPY and CTL tests in Fig. 20f. At most times, the term $T_s[(T_s - T_t)/T_t]$, the effect of the SST and ambient outflow temperature, has made no contribution to the V_{MPI} difference between the two tests, as T_s is identical in CTL and SPY tests, and the difference between the two values of T_t is trivially small (Figs. 20b,f). During the two periods around hour 24 and after hour 57 to the end of the simulation, T_t is larger in the SPY than the CTL test, causing a slightly negative influence. The reason for this is unclear, but may be related to the difference in convective activity. The term C_K/C_D , the ratio between enthalpy and momentum exchange coefficients, mostly contributes to the V_{MPI} difference between the two tests. Before hour 24, when neither of the $V_{m,B}$ values is high, C_K/C_D is slightly smaller in SPY than CTL, making a slightly negative contribution to the magnitude of V_{MPI} in the SPY test. After that time, a large ratio of C_K/C_D in SPY greatly contributes to the large V_{MPI} value in the SPY test (Figs. 20c,f), which also reflects a larger intensification rate in SPY than CTL. The term $\ln \theta_{e,s^*} - \ln \theta_{e,b}$, the effect from the equivalent potential temperatures, is always larger in the SPY test, as a result of an overall smaller $\theta_{e,b}$, especially prior to hour 24 and a larger θ_{e,s^*} after that in SPY than CTL (Figs. 20d,f). The term $\text{CAPE}_s - \text{CAPE}_b$, the effect of two different CAPEs originating from different parcels, is always larger in SPY than in CTL, because of a constant smaller CAPE_b in SPY than in CTL. The CAPE_s results show no systematic difference between the two tests (Figs. 20e,f). Overall, this case study

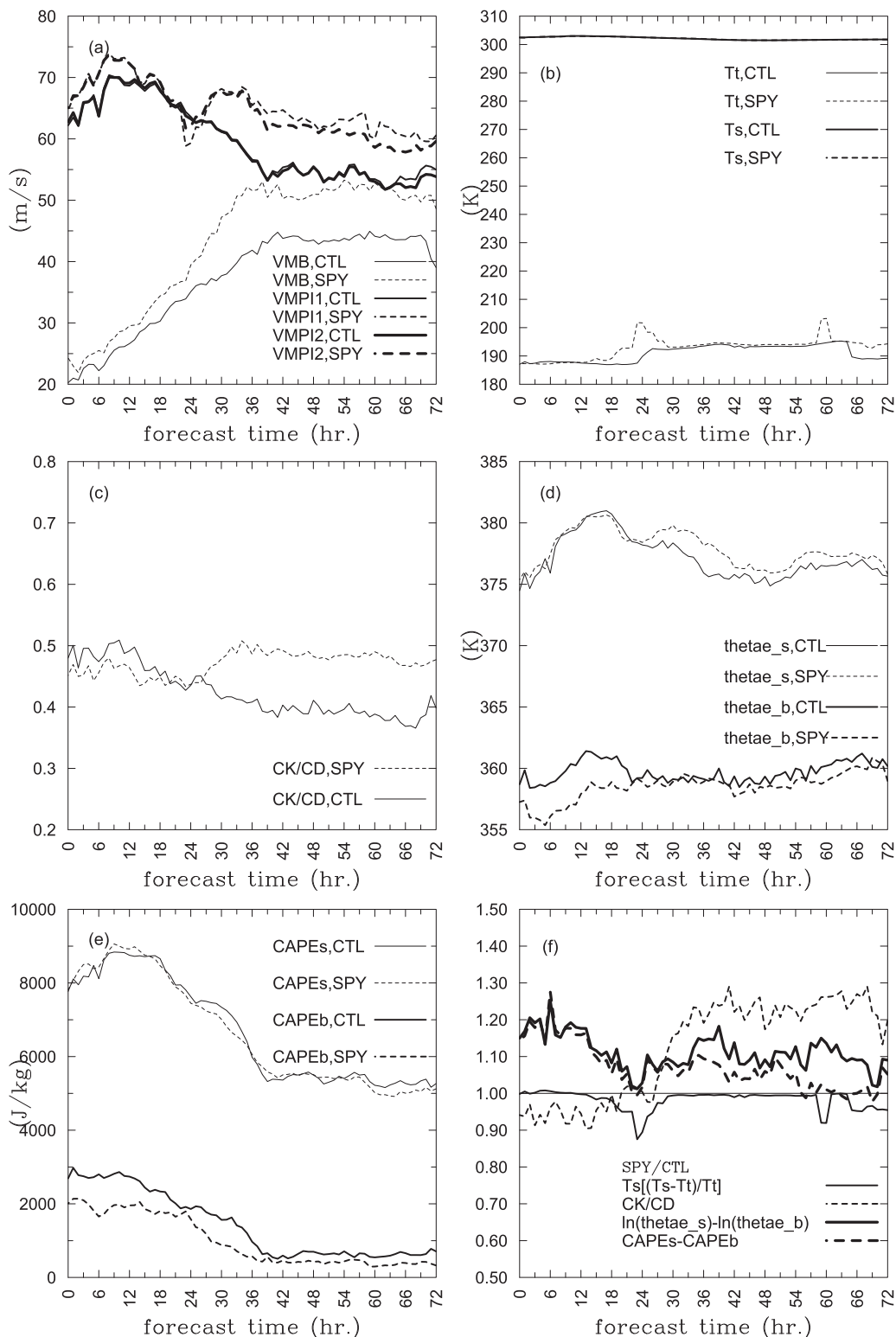


FIG. 20. Time series of V_{MPI} and components contributing to its formation: (a) $V_{m,B}$, V_{MPI1} , and V_{MPI2} . Components constituting the V_{MPI} expressions in Eqs. (11a) and (11b) are (b) T_t and T_s , (c) C_K/C_D , (d) $\theta_{e,s}$ and θ_b , and (e) $CAPE_s$ and $CAPE_b$. (f) Ratios from SPY to CTL tests of $(T_s - T_t)/(T_s/T_t)$, C_K/C_D , $\ln\theta_{e,s} - \ln\theta_b$, and $CAPE_s - CAPE_b$.

shows that, the larger V_{MPI} in SPY compared with CTL is due mainly to a larger value of the ratio of enthalpy and momentum exchange coefficients at high wind speeds, as well as the thermal difference between the sea and hurricane boundary layer that is caused by the sea spray process.

We would attribute the smaller CAPE_b in SPY than CTL to the cooler near-surface air in the SPY test (cf. Figs. 16a and 16b), as a result of the spray evaporation cooling. Although the larger CAPE_b in the CTL could potentially be associated with enhanced convection, the actual larger vertical motion and tangential wind in SPY compared with CTL (cf. Figs. 13a and 13b; see also Fig. 20a) are also influenced by the air–sea interaction processes, which are represented by the MPI theory through its components in Eqs. (11b) and (11c).

5. Conclusions

A revised parameterization for modifying air–sea momentum, sensible heat, and moisture exchanges at high wind speeds has been implemented in the current Australian numerical weather prediction system for tropical cyclones (ACCESS-TC). The parameterization is composed of a sea spray route inclusion scheme for sensible heat and moisture fluxes and a variable Charnock parameter algorithm for momentum roughness length. At high winds of approximately greater than 18 m s^{-1} , the latter not only greatly impacts the parameterization of surface momentum flux but also influences the parameterization of heat and moisture fluxes. The sea spray scheme is adapted from a series of studies summarized in Bao et al. (2011), Fairall et al. (1994), and Kepert et al. (1999), referred to as the BFK model, and is applied in conjunction with the variable Charnock parameter that varies with the 10-m wind speed in neutral conditions. Such a revised air–sea exchange parameterization behaves differently in comparison with the conventional bulk algorithm. At high winds, it has a relatively lower surface stress, enhanced sensible and latent heat fluxes (as well as enthalpy flux), and makes a cooler but moister near-surface layer. Preliminary results suggest the ratio C_K/C_D becomes high with increasingly high winds, which is in general agreement with the theoretical prediction of Emanuel (1986, 1995) for a steady-state tropical cyclone.

For the small number of TC predictions around Australia and the west Pacific conducted so far, the revised air–sea exchange parameterization enhances the predictability of TC intensity, while still mostly maintaining the skill of the track forecasts. In comparison with the bulk algorithm, it enhances the initialized TC circulation during 4DVAR and improves predictions of TC intensity, even for a near steady-state storm.

A rapid intensification case study indicates that the revised parameterization affects the evolution of rapid intensification. Both forecasts represent major features of TC inner-core structure change described in previous studies. A nearly saturated layer with a height of less than 1 km is separated from the surface by a shallow unsaturated mixing layer for both tests. In comparison with the control test using the conventional scheme, the test with the revised scheme predicts a relatively moister and thicker layer above the shallow mixing layer. A more weakly vertically stratified pseudo-potential temperature from the spray route inclusion test seems less inhibiting for subsidence in the eye, which is important to the surface pressure fall. Ultimately, the revised surface fluxes influence the behavior of the eyewall convection, and this in turn appears to influence the behavior of the eyewall and subsidence in the eye. Such behaviors include radial and temporal pulsations of vertical and radial motion in the eye during the RI process.

Regardless of the clear difference in the parameterized surface fluxes in the two simulations, the simulated inner-core structures characterizing rapid intensification and steady-state conditions are basically the same between the two simulations. Both of the simulations represent the positions of inertial instability and vertical motion relative to the radius of the azimuth-mean maximum wind, and the radial divergence and a gradient wind in the layer near the surface. The shapes of the radial profiles of mean relative vorticity are also consistent between the two simulations for both RI and SS. The coherence of the structure change between the schemes implies that it is the TC inner-core dynamics that determines the TC development, while the changes in the surface exchanges modulate the course of the TC development.

Within the framework of Emanuel's MPI theory, the differences between the original and revised air–sea exchange parameterization schemes are characterized mostly by the differences in the ratio between enthalpy and momentum exchange coefficients and the differences in near-surface atmospheric thermal properties. These results lead to the differences between the MPI tangential wind speeds.

Acknowledgments. This research was partially supported by the National Oceanographic Partnership Program (NOPP) and the U.S. Office of Naval Research (ONR) under Award N000141010139.

REFERENCES

- Andreas, E. L., 1992: Sea spray and the turbulent air–sea heat fluxes. *J. Geophys. Res.*, **97**, 11 429–11 441, doi:10.1029/92JC00876.

- , 2010: Spray-mediated enthalpy flux to the atmosphere and salt flux to the ocean in high winds. *J. Phys. Oceanogr.*, **40**, 608–619, doi:10.1175/2009JPO4232.1.
- , 2011: Fallacies of the enthalpy transfer coefficient over the ocean in high winds. *J. Atmos. Sci.*, **68**, 1435–1445, doi:10.1175/2011JAS3714.1.
- , and K. A. Emanuel, 2001: Effects of sea spray on tropical cyclone intensity. *J. Atmos. Sci.*, **58**, 3741–3751, doi:10.1175/1520-0469(2001)058<3741:EOSSOT>2.0.CO;2.
- , P. O. G. Persson, and J. E. Hare, 2008: A bulk turbulent air-sea flux algorithm for high-wind, spray conditions. *J. Phys. Oceanogr.*, **38**, 1581–1596, doi:10.1175/2007JPO3813.1.
- , L. Mahrt, and D. Vickers, 2012: A new drag relation for aerodynamically rough flow over the ocean. *J. Atmos. Sci.*, **69**, 2520–2537, doi:10.1175/JAS-D-11-0312.1.
- Bao, J.-W., J. M. Wilczak, J.-K. Choi, and L. H. Kantha, 2000: Numerical simulations of air–sea interaction under high wind conditions using a coupled model: A study of hurricane development. *Mon. Wea. Rev.*, **128**, 2190–2210, doi:10.1175/1520-0493(2000)128<2190:NSOASI>2.0.CO;2.
- , C. W. Fairall, S. A. Michelson, and L. Bianco, 2011: Parameterizations of sea-spray impact on the air–sea momentum and heat fluxes. *Mon. Wea. Rev.*, **139**, 3781–3797, doi:10.1175/MWR-D-11-00007.1.
- Barnes, G. M., and P. Fuentes, 2010: Eye excess energy and the rapid intensification of Hurricane Lili (2002). *Mon. Wea. Rev.*, **138**, 1446–1458, doi:10.1175/2009MWR3145.1.
- Bell, M. M., M. T. Montgomery, and K. A. Emanuel, 2012: Air–sea enthalpy and momentum exchange at major hurricane wind speeds observed during CBLAST. *J. Atmos. Sci.*, **69**, 3197–3222, doi:10.1175/JAS-D-11-0276.1.
- Bister, M., and K. A. Emanuel, 1998: Dissipative heating and hurricane intensity. *Meteor. Atmos. Phys.*, **65**, 233–240, doi:10.1007/BF01030791.
- Black, P. G., and Coauthors, 2007: Air–sea exchange in hurricanes: Synthesis of observations from the Coupled Boundary Layer Air–Sea Transfers Experiment. *Bull. Amer. Meteor. Soc.*, **88**, 357–374, doi:10.1175/BAMS-88-3-357.
- Bryan, G. H., and R. Rotunno, 2009: The influence of near-surface, high-entropy air in hurricane eyes on maximum hurricane intensity. *J. Atmos. Sci.*, **66**, 148–158, doi:10.1175/2008JAS2707.1.
- Charnock, H., 1955: Wind stress on a water surface. *Quart. J. Roy. Meteor. Soc.*, **81**, 639–640, doi:10.1002/qj.49708135027.
- Chen, J. C. L., and R. T. Williams, 1987: Analytical and numerical studies of the beta-effect in tropical cyclone motion. Part I: Zero mean flow. *J. Atmos. Sci.*, **44**, 1257–1265, doi:10.1175/1520-0469(1987)044<1257:AANSOT>2.0.CO;2.
- Cione, J. J., P. G. Black, and S. H. Houston, 2000: Surface observations in the hurricane environment. *Mon. Wea. Rev.*, **128**, 1550–1561, doi:10.1175/1520-0493(2000)128<1550:SOITHE>2.0.CO;2.
- Csanady, G. T., 2001: *Air–Sea Interaction: Laws and Mechanisms*. Cambridge University Press, 239 pp.
- Davidson, N. E., and Coauthors, 2014: ACCESS-TC: Vortex specification, 4D-VAR initialization, verification, and structure diagnostics. *Mon. Wea. Rev.*, **142**, 1265–1289, doi:10.1175/MWR-D-13-00062.1.
- Davies, T., M. J. P. Cullen, A. J. Malcolm, M. H. Mawson, A. Staniforth, A. A. White, and N. Wood, 2005: A new dynamical core for the Met Office’s global and regional modelling of the atmosphere. *Quart. J. Roy. Meteor. Soc.*, **131**, 1759–1782, doi:10.1256/qj.04.101.
- Donelan, M. A., 1982: The dependence of the aerodynamic drag coefficient on wave parameters. Preprints, *First Int. Conf. on Meteorology and Air–Sea Interaction of the Coastal Zone*, The Hague, Netherlands, Amer. Meteor. Soc., 381–387.
- , B. K. Haus, N. Reul, W. J. Plant, M. Stiassnie, H. C. Graber, O. B. Brown, and E. S. Saltzman, 2004: On the limiting aerodynamic roughness of the ocean in very strong winds. *Geophys. Res. Lett.*, **31**, L18306, doi:10.1029/2004GL019460.
- Drennan, W. M., P. K. Taylor, and M. J. Yelland, 2005: Parameterizing the sea surface roughness. *J. Phys. Oceanogr.*, **35**, 835–848, doi:10.1175/JPO2704.1.
- Dvorak, V. F., 1975: Tropical cyclone intensity analysis and forecasting from satellite imagery. *Mon. Wea. Rev.*, **103**, 420–430, doi:10.1175/1520-0493(1975)103<0420:TCIAAF>2.0.CO;2.
- Edwards, J. M., 2007: Oceanic latent heat fluxes: Consistency with the atmospheric hydrological and energy cycles and general circulation modelling. *J. Geophys. Res.*, **112**, D06115, doi:10.1029/2006JD007324.
- Elsberry, R., T. D. B. Lambert, and M. A. Boothe, 2007: Accuracy of Atlantic and eastern North Pacific tropical cyclone intensity forecast guidance. *Wea. Forecasting*, **22**, 747–762, doi:10.1175/WAF1015.1.
- Emanuel, K. A., 1986: An air–sea interaction theory for tropical cyclones. Part I: Steady-state maintenance. *J. Atmos. Sci.*, **43**, 585–605, doi:10.1175/1520-0469(1986)043<0585:AASITF>2.0.CO;2.
- , 1994: *Atmospheric Convection*. Oxford University Press, 580 pp.
- , 1995: Sensitivity of tropical cyclones to surface exchange coefficients and a revised steady-state model incorporating eye dynamics. *J. Atmos. Sci.*, **52**, 3969–3976, doi:10.1175/1520-0469(1995)052<3969:SOTCTS>2.0.CO;2.
- , 1997: Some aspects of hurricane inner-core dynamics and energetics. *J. Atmos. Sci.*, **54**, 1014–1026, doi:10.1175/1520-0469(1997)054<1014:SAOHIC>2.0.CO;2.
- Fairall, C. W., and S. E. Larsen, 1986: Inertial-dissipation methods and turbulent fluxes at the air–ocean interface. *Bound.-Layer Meteor.*, **34**, 287–301, doi:10.1007/BF00122383.
- , J. D. Kepert, and G. J. Holland, 1994: The effect of sea spray on surface energy transports over the ocean. *Global Atmos. Ocean Syst.*, **2**, 121–142.
- , E. F. Bradley, J. E. Hare, A. A. Grachev, and J. B. Edson, 2003: Bulk parameterization of air–sea fluxes: Updates and verification for the COARE algorithm. *J. Climate*, **16**, 571–591, doi:10.1175/1520-0442(2003)016<0571:BPOASF>2.0.CO;2.
- , M. L. Banner, W. L. Peirson, W. Asher, and R. P. Morison, 2009: Investigation of the physical scaling of sea spray spume droplet production. *J. Geophys. Res.*, **114**, C10001, doi:10.1029/2008JC004918.
- French, J. R., W. M. Drennan, J. A. Zhang, and P. G. Black, 2007: Turbulent fluxes in the hurricane boundary layer. Part I: Momentum flux. *J. Atmos. Sci.*, **64**, 1089–1102, doi:10.1175/JAS3887.1.
- Garratt, J. R., 1994: *The Atmospheric Boundary Layer*. Cambridge University Press, 316 pp.
- Gregory, D., and P. R. Rowntree, 1990: A mass flux convection scheme with representation of cloud ensemble characteristics and stability-dependent closure. *Mon. Wea. Rev.*, **118**, 1483–1506, doi:10.1175/1520-0493(1990)118<1483:AMFCSW>2.0.CO;2.
- Kaplan, J., and M. DeMaria, 2003: Large-scale characteristics of rapidly intensifying tropical cyclones in the North Atlantic basin. *Wea. Forecasting*, **18**, 1093–1108, doi:10.1175/1520-0434(2003)018<1093:LCORIT>2.0.CO;2.

- Kepert, J. D., C. W. Fairall, and J.-W. Bao, 1999: Modelling the interaction between the atmospheric boundary layer and evaporating sea spray droplets. *Air–Sea Exchange—Physics, Chemistry and Dynamics*, G. Geernaert, Ed., Kluwer, 363–410.
- Kossin, J. P., and M. D. Eastin, 2001: Two distinct regimes in the kinematic and thermodynamic structure of the hurricane eye and eyewall. *J. Atmos. Sci.*, **58**, 1079–1090, doi:10.1175/1520-0469(2001)058<1079:TDRITK>2.0.CO;2.
- Large, W. G., and S. Pond, 1982: Sensible and latent heat flux measurements over the ocean. *J. Phys. Oceanogr.*, **12**, 464–482, doi:10.1175/1520-0485(1982)012<0464:SALHFM>2.0.CO;2.
- Liu, B., C. Guan, and L. Xie, 2012: The wave state and sea spray related parameterization of wind stress applicable to from low to extreme winds. *J. Geophys. Res.*, **117**, C00J22, doi:10.1029/2011JC007786.
- Liu, W. T., and J. A. Businger, 1975: Temperature profile in the molecular sublayer near the interface of a fluid in turbulent motion. *Geophys. Res. Lett.*, **2**, 403–404, doi:10.1029/GL002i009p00403.
- Lock, A., 2007: The parameterisation of turbulent fluxes in the boundary layer. UM Documentation Paper 24, Met Office, 55 pp.
- Makin, V. K., 2005: A note on the drag of the sea surface at hurricane winds. *Bound.-Layer Meteor.*, **115**, 169–176, doi:10.1007/s10546-004-3647-x.
- Miyamoto, Y., and T. Takemi, 2013: A transition mechanism for the spontaneous axisymmetric intensification of tropical cyclones. *J. Atmos. Sci.*, **70**, 112–129, doi:10.1175/JAS-D-11-0285.1.
- Montgomery, M. T., J. A. Zhang, and R. K. Smith, 2014: An analysis of the observed low-level structure of rapidly intensifying and mature Hurricane Earl (2010). *Quart. J. Roy. Meteor. Soc.*, **140**, 2132–2146, doi:10.1002/qj.2283.
- Nguyen, M. C., M. J. Reeder, N. E. Davidson, R. K. Smith, and M. T. Montgomery, 2011: Inner-core vacillation cycles during the intensification of Hurricane Katrina. *Quart. J. Roy. Meteor. Soc.*, **137**, 829–844, doi:10.1002/qj.823.
- Powell, M. D., P. J. Vickery, and T. A. Reinhold, 2003: Reduced drag coefficient for high wind speeds in tropical cyclones. *Nature*, **422**, 279–283, doi:10.1038/nature01481.
- Puri, K., and Coauthors, 2013: Implementation of the initial ACCESS numerical weather prediction system. *Aust. Meteor. Oceanogr. J.*, **65**, 265–284.
- Rawlins, F., S. P. Ballard, K. J. Bovis, A. M. Clayton, D. Li, G. W. Inverarity, A. C. Lorenc, and T. J. Payne, 2007: The Met Office global four-dimensional variational data assimilation scheme. *Quart. J. Roy. Meteor. Soc.*, **133**, 347–362, doi:10.1002/qj.32.
- Rogers, R., P. Reasor, and S. Lorsolo, 2013: Airborne Doppler observations of the inner-core structural differences between intensifying and steady-state tropical cyclones. *Mon. Wea. Rev.*, **141**, 2970–2991, doi:10.1175/MWR-D-12-00357.1.
- Schubert, W. H., and J. J. Hack, 1982: Inertial stability and tropical cyclone development. *J. Atmos. Sci.*, **39**, 1687–1697, doi:10.1175/1520-0469(1982)039<1687:ISATCD>2.0.CO;2.
- Smith, R. K., M. T. Montgomery, and V. Nguyen, 2009: Tropical cyclone spin-up revisited. *Quart. J. Roy. Meteor. Soc.*, **135**, 1321–1335, doi:10.1002/qj.428.
- Smith, S. D., 1980: Wind stress and heat flux over the ocean in gale force winds. *J. Phys. Oceanogr.*, **10**, 709–726, doi:10.1175/1520-0485(1980)010<0709:WSAHFO>2.0.CO;2.
- , 1988: Coefficients for sea-surface wind stress, heat flux, and wind profiles as a function of wind speed and temperature. *J. Geophys. Res.*, **93**, 15 467–15 472, doi:10.1029/JC093iC12p15467.
- , and Coauthors, 1992: Sea surface wind stress and drag coefficients: The HEXOS results. *Bound.-Layer Meteor.*, **60**, 109–142, doi:10.1007/BF00122064.
- Van Eijk, A. M. J., B. S. Tranchant, and P. G. Mestayer, 2001: SeaCluse: Numerical simulation of evaporating sea spray droplets. *J. Geophys. Res.*, **106**, 2573–2588, doi:10.1029/2000JC000377.
- Vigh, J. L., and W. H. Schubert, 2009: Rapid development of the tropical cyclone warm core. *J. Atmos. Sci.*, **66**, 3335–3350, doi:10.1175/2009JAS3092.1.
- Wang, Y., and C.-C. Wu, 2004: Current understanding of tropical cyclone structure and intensity changes—A review. *Meteor. Atmos. Phys.*, **87**, 257–278, doi:10.1007/s00703-003-0055-6.
- , and J. Xu, 2010: Energy production, frictional dissipation, and maximum intensity of a numerically simulated tropical cyclone. *J. Atmos. Sci.*, **67**, 97–116, doi:10.1175/2009JAS3143.1.
- , J. D. Kepert, and G. J. Holland, 2001: The effect of sea spray evaporation on tropical cyclone boundary layer structure and intensity. *Mon. Wea. Rev.*, **129**, 2481–2500, doi:10.1175/1520-0493(2001)129<2481:TEOSSE>2.0.CO;2.
- Webster, S., A. R. Brown, D. R. Cameron, and C. P. Jones, 2003: Improvements to the representation of orography in the Met. Office Unified Model. *Quart. J. Roy. Meteor. Soc.*, **129**, 1989–2010, doi:10.1256/qj.02.133.
- Willoughby, H. E., 1998: Tropical cyclone eye thermodynamics. *Mon. Wea. Rev.*, **126**, 3053–3067, doi:10.1175/1520-0493(1998)126<3053:TCET>2.0.CO;2.
- Wilson, M., and S. P. Ballard, 1999: A microphysically based precipitation scheme for the UK Meteorological Office Unified Model. *Quart. J. Roy. Meteor. Soc.*, **125**, 1607–1636, doi:10.1002/qj.49712555707.
- Wu, J., 1980: Wind-stress coefficients over sea surface near neutral conditions—A revisit. *J. Phys. Oceanogr.*, **10**, 727–740, doi:10.1175/1520-0485(1980)010<0727:WSCOSS>2.0.CO;2.
- Yelland, M., and P. K. Taylor, 1996: Wind stress measurements from the open ocean. *J. Phys. Oceanogr.*, **26**, 541–558, doi:10.1175/1520-0485(1996)026<0541:WSMFTO>2.0.CO;2.
- , B. I. Moat, P. K. Taylor, R. W. Pascal, J. Hutchings, and V. C. Cornell, 1998: Wind stress measurements from the open ocean corrected for airflow distortion by the ship. *J. Phys. Oceanogr.*, **28**, 1511–1526, doi:10.1175/1520-0485(1998)028<1511:WSMFTO>2.0.CO;2.
- Zhang, D., and E. Altschuler, 1999: The effects of dissipative heating on hurricane intensity. *Mon. Wea. Rev.*, **127**, 3032–3038, doi:10.1175/1520-0493(1999)127<3032:TEODHO>2.0.CO;2.